On the Phase Nonclosure of Multilook SAR Interferogram Triplets

Francesco Falabella, *Graduate Student Member, IEEE*, and Antonio Pepe, *Senior Member, IEEE*

***Abstract*— This work explores the properties characterizing the phase nonclosure of multilook (ML) synthetic aperture radar (SAR) interferograms. Specifically, we study the implications of ML phase time incongruences on the generation of ground displacement time series through small baseline (SB) multitemporal InSAR (Mt-InSAR) methods. Our research clarifies how these phase inconsistencies can propagate through a time-redundant network of SB interferograms and contribute, along with phase unwrapping (PhU) errors, to the quality of the generated ground displacement products. Moreover, we analyze the effects of short-lived phase bias signals that could happen in sequences of SB interferograms and propose a strategy for their mitigation. The developed methods have been tested using both simulated and real SAR data. The latter were collected by the Sentinel-1 A/B (C-band) sensors over the study areas of Nevada, USA, and Sicily, Italy.**

***Index Terms*— Ground deformations, multitemporal InSAR (Mt-InSAR) algorithms, phase closure.**

I. Introduction

THREE synthetic aperture radar (SAR) images that interfere with each other can generate three interferograms. Several investigations (e.g., [1], [2], [3], [4]) have disclosed a lack of consistency among triplets of interferograms when multilooking operations (or any other statistical procedure, e.g., the noise filtering [5], [6], [7]) are independently applied to every single interferometric SAR data pair. Furthermore, unlike the statistical nature of the nonclosure phase triplets, they have also been related to some underlying systematic physical sources [2], [8]. Some scholars have shown that phase nonclosure signals can bring valuable information on ground properties, for instance, related to the soil moisture content [9], [10], [11], [12], [13], [14], [15], [16], complementing information obtained from the amplitude of SAR images [17].

Manuscript received 28 June 2022; accepted 16 October 2022. Date of publication 21 October 2022; date of current version 22 November 2022. This work was supported in part by the Global Climate Change, Sea Level Rise, Extreme Events and Local Ground Subsidence Effects in Coastal and River Delta Regions Through Novel and Integrated Remote Sensing Approaches (GREENISH) under ESA Project 58351. *(Corresponding author: Antonio Pepe.)*

Francesco Falabella is with the School of Engineering, University of Basilicata, 85100 Potenza, Italy, also with the Institute for Electromagnetic Sensing of the Environment (IREA), National Research Council (CNR) of Italy, 80124 Naples, Italy, and also with the Institute of Methodologies for Environmental Analysis (IMAA), National Research Council (CNR) of Italy, 85050 Tito, Italy (e-mail: francesco.falabella@unibas.it).

Antonio Pepe is with the Institute for Electromagnetic Sensing of the Environment (IREA), National Research Council (CNR) of Italy, 80124 Naples, Italy (e-mail: antonio.pepe@cnr.it).

Digital Object Identifier 10.1109/TGRS.2022.3216083

The phase inconsistencies among a triplet of SAR interferograms have an impact on the retrieval of ground displacement time series through the multitemporal interferometric SAR (Mt-InSAR) techniques [3], [18], [19], [20], [21]. For instance, phase nonclosure triplets might lead to increased phase unwrapping (PhU) errors in a sequence of time-redundant, multitemporal multilook (ML) SAR interferograms because they hinder the time inconsistency of the unwrapped phases [22], [23], [24], [25], [26], [27], [28]. Besides, some advanced Mt-InSAR methods exploit triplets of unwrapped phases to straightforwardly correct PhU errors in sequences of differential SAR interferograms (DInSAR) [25], [29], [30], [31], [32], [33]. Moreover, recent works [34], [35], [36] have claimed that the phase nonclosure signals could lead to a bias in the estimate of the mean ground deformation velocity through small baseline (SB)-oriented Mt-InSAR algorithms. Moreover, some phase bias mitigation approaches have very recently been proposed (see [37], [38]). These methods share some similarities: they exploit long polygon-shaped phase loops and hold the simplified assumption that the phase bias depends on the interferograms temporal baseline (i.e., one phase bias correction for each group of interferograms with a specific temporal baseline).

In our work, we study the properties of phase nonclosure among sets of time-redundant networks of ML SAR interferograms to characterize their effects on the ground displacement time series retrieved using Mt-InSAR SB algorithms. They exploit time-redundant, reduced networks of interferograms with small perpendicular and temporal baselines [19], [21], [31], [39], [40], [41]. We show that a set of stable, coherent pixels at the ML scale, can be suitably identified by analyzing the phase triplets obtained from the selected networks of SB interferograms [42], [43]. Furthermore, a method for estimating and reducing the phase biases into sequences of ML interferograms, relying on the exclusive use of phase triplets, is developed. Experiments were carried out on simulated data and two sets of SAR images collected by the European Copernicus Sentinel-1/A-B (S-1/A-B) sensors over Nevada, USA, and Sicily, Italy. The proposed investigation demonstrates the validity of the developed phase bias mitigation method.

This article is organized as follows. Section II presents the theoretical background of the interferograms' phase nonclosures. Section III proposes a method for phase bias reduction in sequences of ML SB interferograms. Section IV shows some simulations. Section V studies the implications

of noncompensated phase closures for generating interferometric SAR (InSAR) products through SB-oriented Mt-InSAR processing chains. Experimental results are shown in Section VI. Conclusions are finally addressed in Section VII.

II. Phase Triplet's Closure Properties

Let us consider a set of N SAR images collected at the ordered times $\boldsymbol{t} = [t_0, t_1, \ldots, t_{N-1}]^T$ and co-registered to a common reference geometry, and let $\boldsymbol{\Phi} = [\phi_0, \phi_1, \ldots, \phi_{N-1}]^T$ be the (unknown) vector of the full phases (i.e., not restricted to the $[-\pi, \pi]$ range) associated with every single SAR image. Given three interferometric SAR data pairs computed from three generic SAR images collected at times t_h, t_k, t_q (see Fig. 1), the following relation holds:

$$\Delta\phi_{h,k} + \Delta\phi_{k,q} + \Delta\phi_{q,h} = 0 \tag{1}$$

where $\Delta\phi_{n,m} = \phi_m - \phi_n$ is the phase difference between the single-look (SL) SAR images at times t_m and t_n. However, the relation (1) is not applicable when ML interferograms are considered because they involve the estimation of averaged phase values that are independently computed (interferogram by interferogram) over a group of neighboring SAR pixels and they are generally time-inconsistent. In this case, the phase turns out to be a rotational field, see [2] and [44]

$$\Delta\phi^{\mathrm{ML}}_{h,k} + \Delta\phi^{\mathrm{ML}}_{k,q} + \Delta\phi^{\mathrm{ML}}_{q,h} \neq 0 \tag{2}$$

where $\Delta\phi^{\mathrm{ML}}_{n,m} = \Delta\varphi^{\mathrm{ML}}_{n,m} + 2\pi U_{n,m}$ is the phase of the generic (n, m) ML SAR interferogram, $\Delta\varphi^{\mathrm{ML}}_{n,m} = \measuredangle\left\{(1/L)\sum_{\Xi}\exp\left[j(\varphi_m - \varphi_n)\right]\right\}$ is the relevant (wrapped) ML interferometric phase, $U_{n,m}$ is the number of correct (generally unknown) 2π-cycles of the (n, m) unwrapped ML interferogram, and L is the number of looks. Note that $j = \sqrt{-1}$ and $\measuredangle$ is the phase extraction operator; also, Ξ is the group of averaged SAR pixels at the SL scale used to compute the ML interferograms. The (time) rotational phase field in (2) is called a *nonclosure phase triplet*. The excess phase that prevents the closure of the triplet in (2) has different contributions related both to random and systematic sources [1], [2], [34], [44], [45], [46]. The nonclosure phase is a time rotational (i.e., a time-inconsistent) field.

Note that given N SAR images, among the whole possible $N(N-1)/2$ SAR interferograms that can be generated, only $N-1$ are independent. In contrast, the others $(N-1)(N-2)/2$ can be calculated from linear combinations of the previous ones. Multitemporal SB InSAR techniques [18], [47] rely on processing a set of SB ML interferograms $M \leq N(N-1)/2$, which are typically selected by imposing thresholds on the maximum allowed temporal and perpendicular baselines of the SB interferograms. Given such a set of M SB SAR data pairs, a number, say Λ, of phase triplets could then be identified. Specifically, it is worth noting that, considering only a set of SB SAR data pairs, Λ could be noticeably smaller than the maximum number of triplets that can be formed with N SAR images, which is equal to $\Lambda_{\max} = [N(N-1)(N-2)]/6$, of which only $\Lambda_{\text{independent}} = [(N-1)(N-2)]/2$ are independent [2]. We observe that the zth ML phase triplet can be expressed as

$$\begin{aligned}\Delta\phi^{\mathrm{tr}}_z &= \Delta\phi^{\mathrm{ML}}_{h(z),k(z)} + \Delta\phi^{\mathrm{ML}}_{k(z),q(z)} + \Delta\phi^{\mathrm{ML}}_{q(z),h(z)} \\ &= \Delta\varphi^{\mathrm{tr}}_z + 2\pi U_z, \quad z = 0, 1, 2, \ldots, \Lambda - 1\end{aligned} \tag{3}$$

where $\Delta\phi^{\mathrm{tr}}_z$ and $\Delta\varphi^{\mathrm{tr}}_z = W[\Delta\phi^{\mathrm{tr}}_z] \neq 0$ are the zth unwrapped and wrapped nonclosure phase triplet, respectively, U_z is the composite 2π-integer multiple of the zth triplet, and $h(z)$, $k(z)$, and $q(z)$ are the three epochs of the zth triplet. Note also that $W(\cdot)$ is the operator that wraps out the phase into the $[-\pi, \pi]$ range. It can be demonstrated that

$$U_z = U_{h(z),k(z)} + U_{k(z),q(z)} + U_{q(z),h(z)} + U_{h(z),k(z),q(z)} \tag{4}$$

where the last term on the right-hand side of (4)

$$\begin{aligned}&U_{h(z),k(z),q(z)} \\ &\quad = \left[\Delta\varphi^{\mathrm{ML}}_{h(z),k(z)} + \Delta\varphi^{\mathrm{ML}}_{k(z),q(z)} + \Delta\varphi^{\mathrm{ML}}_{q(z),h(z)} - \Delta\varphi^{\mathrm{tr}}_z\right]/2\pi\end{aligned}$$

is the spurious phase cycle arising from the observation that the zth nonclosure phase triplet could exceed $[-\pi, \pi]$. Remarkably, the integer terms in (4) are estimated during the space–time PhU operations (see [22]). Nonetheless, the wrapped phase contribution for the considered triplet $\Delta\varphi^{\mathrm{tr}}_z$ persists, even when PhU operations are perfectly accomplished. If not adequately compensated for, the data vector $\Delta\boldsymbol{\Phi}^{\mathrm{tr}} = [\Delta\varphi^{\mathrm{tr}}_0, \Delta\varphi^{\mathrm{tr}}_1, \ldots, \Delta\varphi^{\mathrm{tr}}_{\Lambda-1}]^T$ might influence the quality of the Mt-InSAR results (i.e., the ground deformation time series and the relevant mean ground deformation velocity maps) obtained after inverting the sequence of unwrapped ML interferograms $\Delta\boldsymbol{\Phi} = [\Delta\phi_0, \Delta\phi_1, \ldots, \Delta\phi_{M-1}]^T$.

A. ML Speckle Noise Model

The mentioned phase triplets' inconsistencies $\Delta\boldsymbol{\Phi}^{\mathrm{tr}}$ could arise, for instance, when in the ML averaging box, different populations of scatterers, characterized by independent phase histories, interfere with one another [9]. Indeed, both the spatial and the temporal inconsistency in the ML averaging window can give rise to nonzero closure phases [38]. To investigate the origin of these phase inconsistencies, let us consider the nth phase triplet, namely $\Delta\varphi^{\mathrm{tr}}_n$, which involves the three SAR images collected at times (t_h, t_k, t_q), see Fig. 1. First, let us focus on the (t_h, t_k) SAR data pair and consider a scenario with F independent populations of scatterers in the averaging window. The generic fth scatterers' population can be assumed, for the sake of simplicity, to have only two independent phase contributions:[1] the (averaged) true ground deformation signal, namely, $\Delta\phi^{\mathrm{ML,defo}}_{h,k}$, and an inherent phase term that characterizes a specific, local physical property of the scatterers, namely, $\Delta\phi^{\mathrm{ML},f}_{h,k}$. Given the two complex-valued SAR images S_h and S_k forming the relevant (h, k) interferogram, the ML speckle noise model for the Hermitian product $S_h S_k^*$ developed by López-Martínez and Pottier [48]

[1]Other time-consistent, nonlocal phase signals that are common to all families of scatterers (such as the topographic residuals and orbital phase artifacts) can be seen included in the ground deformation phase term.

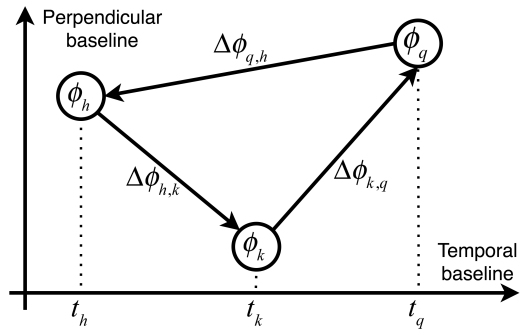

Fig. 1. Pictorial representation of a generic interferometric phase triplet in the temporal/perpendicular baseline plane. The nodes highlight the ith SAR image (gathered at times t_h, t_k, and t_q), whereas the three arcs represent the interferometric phases.

can be adopted

$$\begin{aligned}\left\langle S_h S_k^* \right\rangle_L &= \sum_{f=1}^{F} \left\langle S_h S_k^* \right\rangle_{L_f} \\ &= \sum_{f=1}^{F} \left\{ \begin{array}{l} \psi_f \rho_f \exp\left[j\left(\Delta\phi_{h,k}^{\mathrm{ML,defo}} + \Delta\phi_{h,k}^{\mathrm{ML},f} \right) \right] \\ + \psi_f \left(n_{m,f} - N_{c,f} \bar{z}_{L_f} \right) \\ \times \exp\left[j\left(\Delta\phi_{h,k}^{\mathrm{ML,defo}} + \Delta\phi_{h,k}^{\mathrm{ML},f} \right) \right] \\ + \psi_f \left(n_{ar,f} + j n_{ai,f} \right) \end{array} \right\} \end{aligned} \quad (5)$$

where the symbol $\langle\cdot\rangle_L$ denotes the spatial average operation computed over L samples, in which $L = \sum_{f=1}^{F} L_f$. Moreover, $\Xi = \bigcup_{f=1}^{F} \Xi_f$ is the partition of the group of pixels Ξ of the averaging window into F independent subgroups, representing the relevant scatterers' populations, with every single set Ξ_f with L_f looks. We remark that $\psi_f \rho_f \exp[j(\Delta\phi_{h,k}^{\mathrm{ML,defo}} + \Delta\phi_{h,k}^{\mathrm{ML},f})]$ is the true, expected signal component related to the fth population, with ρ_f being the corresponding coherence value of the scatterer's family. Moreover, $n_{m,f}$ is a multiplicative noise component, $N_{c,f} \cong 1 - 1/(8L_f)$, and $\bar{z}_{L_f}$ is defined in [48], where $E[n_{m,f} - N_{c,f}\bar{z}_{L_f}] = 0$ and $\mathrm{var}[n_{m,f}] = N_{c,f}^2 \left[\left(1 + |\rho_f|^2\right)/2L_f \right]$. Note that $E[\cdot]$ is the statistical expectation operator. Finally, $n_{ar,f} + j n_{ai,f}$ is a complex-valued additive noise term with $E[n_{ar,f}] = E[n_{ai,f}] = 0$ and variance $\mathrm{var}[n_{ar,f}] = \mathrm{var}[n_{ai,f}] = (1/2L_f)(1 - |\rho_f|^2)^{1.32(L_f)^{1/2}}$. Of course, in order to describe the characteristics of the scatterers' families involved in the ML window, other speckle noise models, such as the one proposed in [38], might be applied.

Accordingly, considering the speckle noise model described by (5), the ML (expected) phase related to the (h,k) interferometric SAR data pair can be expressed as

$$\begin{aligned}\Delta\varphi_{h,k}^{\mathrm{ML}} &= \measuredangle \left\langle S_h S_k^* \right\rangle_L \\ &= W\left\{ \Delta\varphi_{h,k}^{\mathrm{ML,defo}} + \measuredangle \left[\sum_{f=1}^{F} \psi_f \rho_f e^{j\Delta\phi_{h,k}^{\mathrm{ML},f}} \right] + \zeta_{h,k} \right\} \end{aligned} \quad (6)$$

where $\zeta_{h,k}$ is a resulting zero-mean additive noise phase term.

As a first approximation, we can assume that the model in (6) depends only on the temporal baseline of the considered (t_h, t_k) SAR data pair $\Delta t_{h,k} = |t_k - t_h|$. Under this simplified hypothesis, $\rho_f = \rho_f(t_h, t_k) = \rho_f(|t_k - t_h|)$, $\Delta\phi_{h,k}^{\mathrm{ML},f}(t_h, t_k; |t_k - t_h|) = \Delta\phi_{h,k}^{\mathrm{ML},f}(|t_k - t_h|)$, and $\psi_f = \psi_f(t_h, t_k; |t_k - t_h|) = \psi_f(|t_k - t_h|)$. Concerning the temporal decorrelation models that describe how the coherence depends on the interferometric temporal baseline, interested readers are referred to the literature, see, for instance, [49], [50], and [51].

In Section III, we then relax these hypotheses to consider a more general time-variant case. Space–time, physical and statistical properties of local, inherent signals that contribute to the systematic phase biased signal $\measuredangle[\sum_{f=1}^{F} \psi_f \rho_f e^{j\Delta\phi_{h,k}^{\mathrm{ML},f}}]$ can be found in the literature. For instance, readers are referred to [9], [11], [12], [14], [15], [16], [52], and [53] to have a comprehensive analysis of the models adopted for the characterization of soil moisture content variations and its impact on InSAR investigations. We would like to remark that, in our work, we do not want to discriminate one another the different inherent, local signals $\Delta\phi_{h,k}^{\mathrm{ML},f}, \forall f$ that contribute to the phase biased signal nor the time series of the inherent phase contributions. Conversely, we want to estimate and mitigate the effect of the "composite" global systematic phase biased components $\Delta\varphi_{h,k}^{\mathrm{bias}} = \measuredangle \sum_{f=1}^{F} \psi_f \rho_f e^{j\Delta\phi_{h,k}^{\mathrm{ML},f}}$ on the ground deformation products, as obtained using Mt-InSAR algorithms (e.g., [18], [19], [39], [47], [54]).

Experimental results have evidenced that the systematic phase bias $\Delta\varphi_{h,k}^{\mathrm{bias}} = \measuredangle \sum_{f=1}^{F} \psi_f \rho_f e^{j\Delta\phi_{h,k}^{\mathrm{ML},f}}$ is a short-lived signal that rapidly decays as the temporal baseline increases [34], [36], [37], [38], [55]. For small values of $\Delta t_{h,k} = |t_k - t_h|$, we can locally expand the (full) phase bias related to the (h,k) interferogram $\Delta\phi_{h,k}^{\mathrm{bias}}$ as

$$\Delta\phi_{h,k}^{\mathrm{bias}}\left(\Delta t_{h,k}\right) \cong \left[v + \Delta v\left(\Delta t_{h,k}\right) \right] \Delta t_{h,k} \quad (7)$$

where v is a constant decay phase velocity factor and $\Delta v(\Delta t_{h,k})$ is a temporal-baseline-dependent phase velocity difference term. Using (6) and (7), the nth phase triplet $\Delta\varphi_n^{\mathrm{tr}}$ can be expressed as follows:

$$\begin{aligned}\Delta\varphi_n^{\mathrm{tr}} &= W\left[\Delta\phi_{h,k}^{\mathrm{ML}} + \Delta\phi_{k,q}^{\mathrm{ML}} + \Delta\phi_{q,h}^{\mathrm{ML}} \right] \\ &= W\left[\Delta\phi_{h,k}^{\mathrm{bias}} + \Delta\phi_{k,q}^{\mathrm{bias}} + \Delta\phi_{q,h}^{\mathrm{bias}} \right] + \zeta_{h,k,q} \\ &\cong W\left[\Delta v\left(\Delta t_{h,k}\right)\Delta t_{h,k} + \Delta v\left(\Delta t_{k,q}\right)\Delta t_{k,q} - \Delta v\left(\Delta t_{h,q}\right)\Delta t_{h,q} \right] \\ &\quad + \zeta_{h,k,q} \end{aligned} \quad (8)$$

where $\zeta_{h,k,q}$ is the zero-mean random noise phase term related to the (t_h, t_k, t_q) interferometric triplet. From (8), the (wrapped) triplet systematic phase bias can be expressed as $\Delta\phi_{h,k,q}^{\mathrm{bias}} = \Delta v(\Delta t_{h,k})\Delta t_{h,k} + \Delta v(\Delta t_{k,q})\Delta t_{k,q} - \Delta v(\Delta t_{h,q})\Delta t_{h,q}$, which solely depends on the velocity difference terms $\Delta v(\Delta t_{i,j})$ $i, j = h, k, q$ and is insensitive to the mean constant decay velocity factor v. Because the phase bias is a short-lived signal, with significant phase rates only at very small temporal baselines and negligible rates at medium-to-long baselines, it is reasonably assumed that $|\Delta\phi_n^{\mathrm{tr}}| \leq \pi$ (see [9]). On the other hand, using polygons of interferograms (see [37], [38]), the probability that the absolute value of the nonclosure phases could exceed π increases as the number of polygon sides increases. This probability is assumed low in [37], and however, in the case that these long phase loops

exceed π in moduli, there would be a corrupt estimate and compensation of the bias. On the contrary, in [38], the phase-unwrapping operations are performed on the nonclosure phase loops. In this case, some (unavoidable) PhU errors committed could potentially degrade, to some extent, the reliability of the estimation and compensation of the phase bias.

B. Statistical Properties of the Phase Triplets

Given a set of N SAR images, the selected M SB SAR interferograms can be arranged to form Λ triplets. For every radar pixel, the vector of the (wrapped) phase triplet $\Delta\boldsymbol{\Phi}^{\text{tr}} = [\Delta\varphi_0^{\text{tr}}, \Delta\varphi_1^{\text{tr}}, \ldots, \Delta\varphi_{\Lambda-1}^{\text{tr}}]^T$ is a multisample random circular data vector whose elements have different statistics, depending on the geometrical characteristics of the different families of triplets that could be formed. For instance, if we consider the family of interferometric triplets made by three Sentinel-1 SAR interferograms with temporal baselines of 6, 6, and 12 days, the corresponding systematic phase bias signal $\Delta\phi^{\text{bias}}_{\Delta t_{h,k},\Delta t_{k,q},\Delta t_{h,q}} = \Delta v(\Delta t_{h,k})\Delta t_{h,k} + \Delta v(\Delta t_{k,q})\Delta t_{k,q} - \Delta v(\Delta t_{h,q})\Delta t_{h,q}$ equals $\Delta\phi^{\text{bias}}_{6,6,12} = [\Delta v(6) - \Delta v(12)]12$. In general, when the family of interferometric triplets with temporal baselines of $\Delta t_{h,k} = \Delta t_{k,q}$ and $\Delta t_{h,q} = 2\Delta t_{h,k}$ is concerned, the relevant systematic phase bias equals: $\Delta\phi^{\text{bias}}_{\Delta t_{h,k},\Delta t_{h,k},2\Delta t_{h,k}} = 2[\Delta v(\Delta t_{h,k}) - \Delta v(2\Delta t_{h,k})]\Delta t_{h,k}$. Therefore, under the simplified hypothesis that the model in (6) is invariant with time, the set of Λ triplets, namely, $\text{Tr} \equiv \{\text{Tr}_n\}_{n=1}^{\Lambda}$, can be partitioned as $\text{Tr} = \bigcup_{\chi=1}^{\text{X}} \text{Tr}_\chi$, where X is the number of different homogeneous families of interferometric triplets.[2] Let us now consider the generic family Tr_χ, composed of Λ_χ elements, and the phase vector $\Delta\boldsymbol{\Phi}_\chi^{\text{tr}} = [\Delta\varphi_{\chi,0}^{\text{tr}}, \Delta\varphi_{\chi,1}^{\text{tr}}, \ldots, \Delta\varphi_{\chi,\Lambda_\chi-1}^{\text{tr}}]^T$. It can be demonstrated that the elements of the vector $\Delta\boldsymbol{\Phi}_\chi^{\text{tr}}$ are Von Mises-distributed $\text{VM}(\mu_\chi, \kappa_\chi)$, with an averaged phase value μ_χ and a concentration parameter κ_χ [56]

$$\mu_\chi = \Delta\phi_\chi^{\text{bias}} = \text{atan}\left[\frac{\sum_{i=0}^{\Lambda_\chi-1}\sin\left(\Delta\varphi_{\chi,i}^{\text{tr}}\right)}{\sum_{i=0}^{\Lambda_\chi-1}\cos\left(\Delta\varphi_{\chi,i}^{\text{tr}}\right)}\right] \tag{9}$$

$$\kappa_\chi \cong \frac{1}{2\left(1-\Gamma_\chi\right)} \tag{10}$$

where Γ_χ is the (sample) mean resultant length of the χth family of phase triplets

$$\Gamma_\chi = \frac{1}{\Lambda_\chi}\left|\sum_{i=0}^{\Lambda_\chi-1}\exp\left[j\,\Delta\varphi_{\chi,i}^{\text{tr}}\right]\right|. \tag{11}$$

Equations (9)–(11) show that the systematic bias of the considered family of triplets is the mean direction of the phase triplets' distribution μ_χ, whereas the mean resultant length Γ_χ gives us a measure of the spread of the phase triplets with respect to μ_χ, accounting for the zero-mean random noise contribution $\zeta_{h,k,q}$. The first-order statistics of the amplitude and phase of the directional random data $\sum_{i=0}^{\Lambda_\chi-1}\exp[j\,\Delta\varphi_{\chi,i}^{\text{tr}}] = R_\chi\exp[j\,\Delta\Phi_\chi]$ are derived in Appendix I. It can be demonstrated that the standard deviation of the χth phase triplet family is given by

$$\text{var}\left(\Phi_\chi\right) \cong \frac{2\left(1-\Gamma_\chi\right)\left(2-\Gamma_\chi\right)}{\Lambda_\chi}. \tag{12}$$

The mean resultant length of the combined multisample data vector $\Delta\boldsymbol{\Phi}^{\text{tr}} = [\Delta\varphi_0^{\text{tr}}, \Delta\varphi_1^{\text{tr}}, \ldots, \Delta\varphi_{\Lambda-1}^{\text{tr}}]^T$ is eventually given by

$$\Gamma_{\text{triang}} = \frac{1}{\Lambda}\left|\sum_{i=0}^{\Lambda-1}\exp\left[j\,\Delta\varphi_i^{\text{tr}}\right]\right| = \left|\sum_{\chi=1}^{\text{X}}\Gamma_\chi\exp\left[j\,\mu_\chi\right]\right| \in [0,1] \tag{13}$$

which is referred in this work to as the triangular coherence of the identified network of SB ML interferograms. We remark that Γ_{triang} can be seen as an equivalent coherence [57] and gets a direct measure of the nonclosure (overall) phase triplets' dispersion to its mean value.

The triangular coherence can be used to select a group of reliable, coherent SAR pixels at the ML scale. Indeed, the triangular coherence gets a measure of the noise level that affects the selected set of ML interferograms. In particular, the mean resultant length of the phase triplets $\Delta\boldsymbol{\Phi}^{\text{tr}} = [\Delta\varphi_0^{\text{tr}}, \Delta\varphi_1^{\text{tr}}, \ldots, \Delta\varphi_{\Lambda-1}^{\text{tr}}]^T$ is asymptotically normal with $\sigma^2_{\text{triang}} \cong (1-\Gamma^2_{\text{triang}})/\Lambda$ (see Mardia and Jupp's book [56]). Accordingly, the variance of this estimator drastically decreases as the number of triplets Λ and the triangular coherence value Γ_{triang} increase. The group of coherent SAR pixels is thus straightforwardly identified by simply imposing a threshold γ_{triang} on the minimum triangular coherence value of the analyzed pixel, as $\Theta \equiv \{P : \Gamma_{\text{triang}}(P) \geq \gamma_{\text{triang}}\}$.

III. Phase Bias Estimation and Mitigation

This section presents a method to estimate the phase bias affecting a sequence of SB ML interferograms characterized by the maximum temporal baseline $\Delta t_{\max}$.

A. Time-Invariant Case

Let us first assume that the model of (6) is time-invariant, i.e., $\Delta\phi^{\text{bias}}_{h,k}(t_h, t_k) = \Delta\phi^{\text{bias}}_{h,k}(\Delta t_{h,k})\ \forall h,k$. Under this hypothesis, the expansion given by (7) is suitable. We remark that the temporal baseline of an interferogram is a multiple of the sampled temporal revisit time of the used SAR sensor, namely, δ, which, for instance, is equal to six days for the twin constellations of Sentinel-1 A/B sensors. Accordingly, if we consider two generic interferometric SAR data pairs with temporal baselines $(\lambda-1)\delta$ and $\lambda\delta$, with $\lambda \in \mathbb{Z}$, (7) particularizes as

$$\Delta\phi^{\text{bias}}(\lambda\delta) \cong [v + \Delta v(\lambda\delta)]\lambda\delta \tag{14}$$

$$\Delta\phi^{\text{bias}}[(\lambda-1)\delta] \cong \{v + \Delta v[(\lambda-1)\delta]\}(\lambda-1)\delta. \tag{15}$$

Comparing (14) and (15), the following iterative relation is derived:

$$\Delta\phi^{\text{bias}}[(\lambda-1)\delta] \cong \frac{\lambda-1}{\lambda}\Delta\phi^{\text{bias}}(\lambda\delta) + \{\Delta v[(\lambda-1)\delta] - \Delta v(\lambda\delta)\}(\lambda-1)\delta. \tag{16}$$

[2]Note that the hypothesis on the homogeneity of the phase triplet families is subsequently relaxed in Section III.

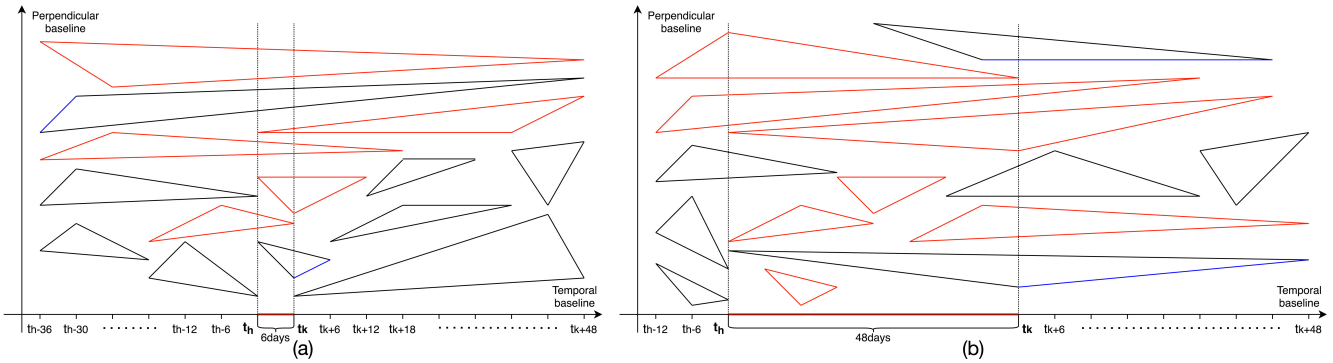

Fig. 2. Simulations related to the time-variant case: Pictorial representation of allowed (red color) and not allowed (black color) triplets, considering a time window of (a) 6 days and (b) 48 days, respectively. The arcs with the same time duration as the reference window (dark red) are highlighted in blue, as they do not satisfy the second condition and the relevant triangles must be excluded.

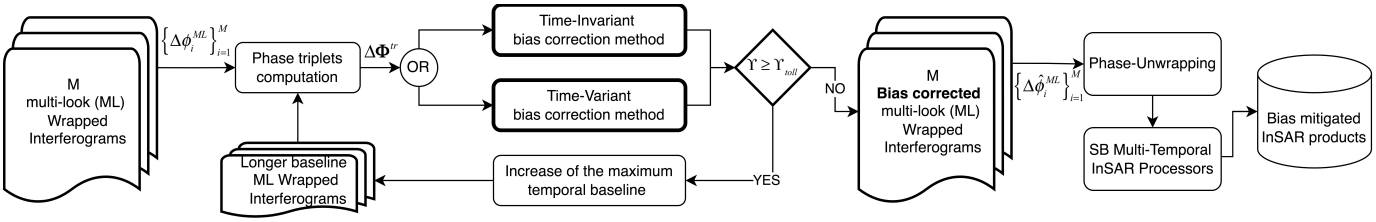

Fig. 3. Flow diagram of the proposed bias estimation and mitigation algorithm.

Equation (8) defines a system of Λ linear equations with respect to the (unknown) phase bias velocity differences $\Delta \boldsymbol{V} = [\Delta v(\delta), \Delta v(2\delta), \ldots, \Delta v(k\delta), \ldots, \Delta v(\Delta t_{\max})]^T$

$$\Delta \boldsymbol{\Phi}^{\mathrm{tr}} = \boldsymbol{Z} \cdot \Delta \boldsymbol{V} \tag{17}$$

that can be solved in the least-squares (LS) sense as $\Delta \hat{\boldsymbol{V}} = \boldsymbol{Z}^{\dagger} \cdot \Delta \boldsymbol{\Phi}^{\mathrm{tr}}$, where $\boldsymbol{Z}^{\dagger}$ is the pseudoinverse of the matrix $\boldsymbol{Z}$; the symbol $\cdot$ stands for the matrix multiplication (rows by columns) operator. Then, the estimates $\Delta \hat{\boldsymbol{V}}$ are used to iteratively compute the phase biases at the different temporal baselines $\Delta t_{\lambda} = \lambda\delta$, $\forall \lambda = 1, 2, \ldots, \Delta t_{\max}/\delta$ through (16) using the initial condition $\Delta\phi^{\mathrm{bias}}(\Delta t_{\max}) = 0$. As claimed in several independent investigations [34], [36], [37], [38], the phase bias is a signal that rapidly decays as the temporal baseline increases. However, it is not guaranteed that the maximum temporal baseline $\Delta t_{\max}$ of the selected set of SB interferograms is large enough to assume that $\Delta\phi^{\mathrm{bias}}(\Delta t_{\max}) = 0$. A strategy to understand whether the maximum temporal baseline $\Delta t_{\max}$ is adequate for the phase bias correction is to compute, and for every single SAR pixel of the scene, the term $\Upsilon = |\Delta v(\Delta t_{\max} - \delta) - \Delta v(\Delta t_{\max})|$. If Υ is larger than a given tolerance Υ_{toll} (e.g., $\Upsilon \geq 10^{-4}$), some additional interferograms with longer baselines must then be added. It is worth remarking that the additional long-baseline ML interferograms are exclusively used to compute the phase bias. However, they are not exploited to generate the ground deformation time series using an SB-oriented algorithm [18], [19], [39], [47], [54].

B. Time-Variant Case

Let us now assume that the model of (6) is time-variant, i.e., $\Delta\phi^{\mathrm{ML}}_{h,k} = \Delta\phi^{\mathrm{ML}}_{h,k}(t_h, t_k)$. In this case, the strategy described in Section III-A can be specialized by locally applying it to single time windows, by dynamically selecting and using only subgroups of triplets' families that encompass the selected time window to estimate the phase bias. To describe the developed method, let us focus on the generic ith ML SAR interferogram that spans the time window between the times t_h and t_k of duration $m_{h,k}\delta$. The phase bias estimate related to this ith interferogram is carried out by using (17) considering only the triplets $\{\alpha, \beta, \gamma\}$ (see Fig. 2) that satisfy both the following conditions.

1) At least one of the three arcs $\{\alpha, \beta, \gamma\}$ of the given triplet must wholly be included or include the reference time window $[t_h, t_k]$.
2) For all the three arcs: the generic arc of the triplet is the reference time window $[t_h, t_k]$ or its duration is different from the reference time window duration.

Fig. 2 shows some pictorial examples of allowed and not allowed (discarded) triplets, considering as a reference a time window of 6 days [see Fig. 2(a)] and 48 days [see Fig. 2(b)]. Then, the phase bias estimates $\Delta\phi^{\mathrm{bias}}_{h,k}$ are used to exclusively correct the ith ML SB interferogram as: $\Delta\hat{\phi}^{\mathrm{ML}}_i = W(\Delta\phi^{\mathrm{ML}}_i - \Delta\phi^{\mathrm{bias}}_{h,k})$. The block diagram of the proposed phase bias correction method is shown in Fig. 3.

C. Compensation of the Random Phase Signal Components

Once the systematic phase bias components are estimated and compensated for, however, some uncompensated time-inconsistent random phase noise contributions, which lead to phase nonclosures, can persist. They can effectively be compensated for using the methods described in [1], [3], [4], [46], [58], [59], [60], and [61]. In particular, the application of the first step of the extended minimum cost flow (EMCF)-based processing chain [3], which is fully detailed in [57] and here referred to as enhanced multitemporal noise-filtering (E-Mt-InSAR) algorithm, allows one to obtain a set

of optimized, fully time-consistent set of ML SAR interferograms. More specifically, for every SAR pixel of the ML grid, the E-Mt-InSAR method is based on searching for the (unknown) phase vector of the wrapped phases related to the available N SAR acquisitions that minimize the (weighted) circular variance of the random phase vector representative of the difference between the original and the optimized interferograms reconstructed from the computed (wrapped) phases associated with every SAR acquisition (i.e., the residual phases). It is worth remarking that the (weighted) circular variance gets a measure of the dispersion of the residual phases about their (weighted) mean direction. However, no constraint is imposed about the mean (weighted) direction of the residual phases, and the estimator is not able to adequately discriminate between the short-lived systematic phase contributions and the zero-mean random phases associated with the ML SB interferograms, see also the experimental results shown in Appendix II. An effective strategy that could be adopted is, first, to compensate/mitigate the systematic phase bias components using the algorithms described in Sections III-A and III-B and then apply the E-Mt-InSAR noise-filtering algorithm to the set of compensated ML interferograms $\{\Delta\hat{\phi}_i^{\mathrm{ML}}\}_{i=1}^{M}$. Accordingly, using this strategy, both the systematic and random noise phase contributions can be adjusted.

D. Role of PhU Errors

The presented analyses do not consider the effects of biased time-inconsistent PhU errors. As a matter of fact, once the ML interferograms are unwrapped, some of the observed discrepancies in the generated InSAR products can also be due to time-polarized PhU errors, e.g., 2π-multiples PhU errors that are superimposed on phase triplets and are responsible for time incongruences that can propagate through the selected network of SB interferograms. These effects arise when the SB interferograms are unwrapped independently [62], [63], [64], [65] and/or using some hybrid 2-D + 2-D space–time PhU methods [22], [26], [28] that do not ensure that the PhU solution is time-irrotational. These effects are appropriately considered by the temporal coherence factor, which is computed after the SB inversion of the unwrapped interferograms, as detailed in Section V. Hence, the temporal coherence value is used to detect those pixels that are more affected by time-inconsistent phase artifacts and exclude them from the subsequent analyses.

IV. Simulation

The developed phase bias correction method was first tested in a controlled environment by running some simulations. Specifically, we have considered the following cases: 1) the model (6) is time-invariant (see Section III-A) and 2) the model (6) is time-variant where the nonstationary phase correction method described in Section III-B is applied. For both cases, we have also considered the effects of the decorrelation noise that has been introduced in the test environment.

A. Time-Invariant Case

In this first case, the assumption is retained that the phase bias depends only on the time span of the considered InSAR data pair, i.e., $\Delta\phi_{h,k}^{\mathrm{bias}} = \Delta\phi_{h,k}^{\mathrm{bias}}(t_h, t_k) = \Delta\phi_{h,k}^{\mathrm{bias}}(\Delta t_{h,k})$, where t_h and t_k are the two generic time acquisitions. The simulation has been carried out considering the time distribution and the SB interferometric network settings related to the Nevada case-study area (see Section V). We considered $N = 65$ SAR acquisitions and $M = 895$ SB InSAR data pairs selected by imposing a maximum temporal baseline $\Delta t_{\max} = 96$ days. The interferograms' temporal baselines are sampled as: $\Delta\mathbf{t} = \{\Delta t_{\max}/d_S, \Delta t_{\max}/d_{S-1}, \ldots, \Delta t_{\max}/d_1\}$, where $\{d_S = (\Delta t_{\max}/6) = 16, d_{S-1} = 15, \ldots, d_2 = 2, d_1 = 1\}$. Considering the selected network of M SB ML interferograms, $\Lambda = 6305$ InSAR triplets have been identified. By referring to the phase model described by (6), we assumed the presence of $F = 2$ independent populations of scatterers in the averaging ML spatial window and for the sake of simplicity that $\Delta\varphi_{h,k}^{\mathrm{ML,defo}} = 0 \ \forall h, k$. First, a free-noise scenario was assumed, i.e., $\zeta_{h,k} = 0 \ \forall h, k$. In this case, the adopted InSAR phase model (6) particularizes as: $\Delta\varphi_{h,k}^{\mathrm{ML}} = W\{\angle[\psi_1\rho_1 e^{j\Delta\phi_{h,k}^{\mathrm{ML},1}} + \psi_2\rho_2 e^{j\Delta\phi_{h,k}^{\mathrm{ML},2}}]\}$. For the first family of scatterers, we set $\Delta\phi_{h,k}^{\mathrm{ML},1} = 0$, $\rho_1 = 1$, and $\psi_1 = 1$. Differently, for the second family of scatterers, the following values are set: $\Delta\phi_{h,k}^{\mathrm{ML},2} = \xi\,\Delta t_{h,k}$, $\rho_2 = e^{-\alpha\,\Delta t_{h,k}}$, and $\psi_2 = 1$, where $\alpha = (11/2)(1/\Delta t_{\max})$ and $\xi = q\pi(1/\Delta t_{\max})$. Fig. 4 shows the plots of simulated inherent (independent) phase term for the second family of scatterers versus the interferograms temporal baseline, considering the two cases with $q = 1$ and 4. In this round of simulations, we have assumed that the average phase of the second family varies linearly with time and $\rho_2 = e^{-\alpha\,\Delta t_{h,k}}$ in accordance with the temporal decorrelation models proposed in the literature (see [50]). In such a way, the made hypothesis that model (6) is time-invariant is valid. Based on the parameters listed above, the adopted InSAR phase model becomes: $\Delta\varphi_{h,k}^{\mathrm{ML}} = W\{\angle[1 + e^{-\alpha\,\Delta t_{h,k}} e^{j\xi\,\Delta t_{h,k}}]\}$.

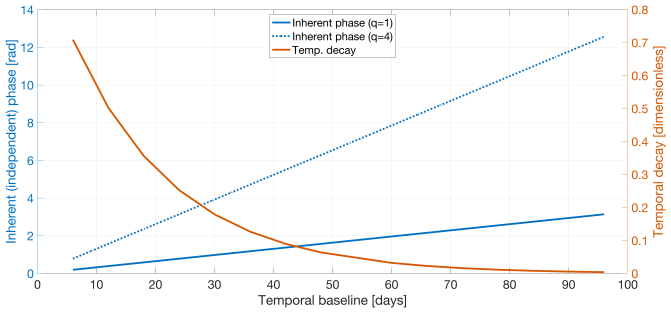

Fig. 4. Simulated values for the InSAR phase model (6), referred to the second family of scatterers. The inherent (independent) phase terms $\Delta\phi_{h,k}^{\mathrm{ML},2}$ for $q = 1$ and 4, respectively, are plotted in blue with solid and dashed lines, while in orange, the coherence temporal decay ρ_2 is plotted. The plots are functions of the InSAR temporal baselines.

The simulated phases, which are plotted versus the temporal baseline (blue lines) in Fig. 5(a) and (b), correspond to a maximum (simulated) phase bias velocity of roughly 2.1 and 8.7 cm/year, related to InSAR data pairs with a temporal baseline of $\Delta t = 6$ days and assuming a wavelength of 5.546 cm (i.e., that of Sentinel-1 A/B), for the simulations with $q = 1$ and 4, respectively. We have applied the phase bias estimation method described in Section III-A to simulated

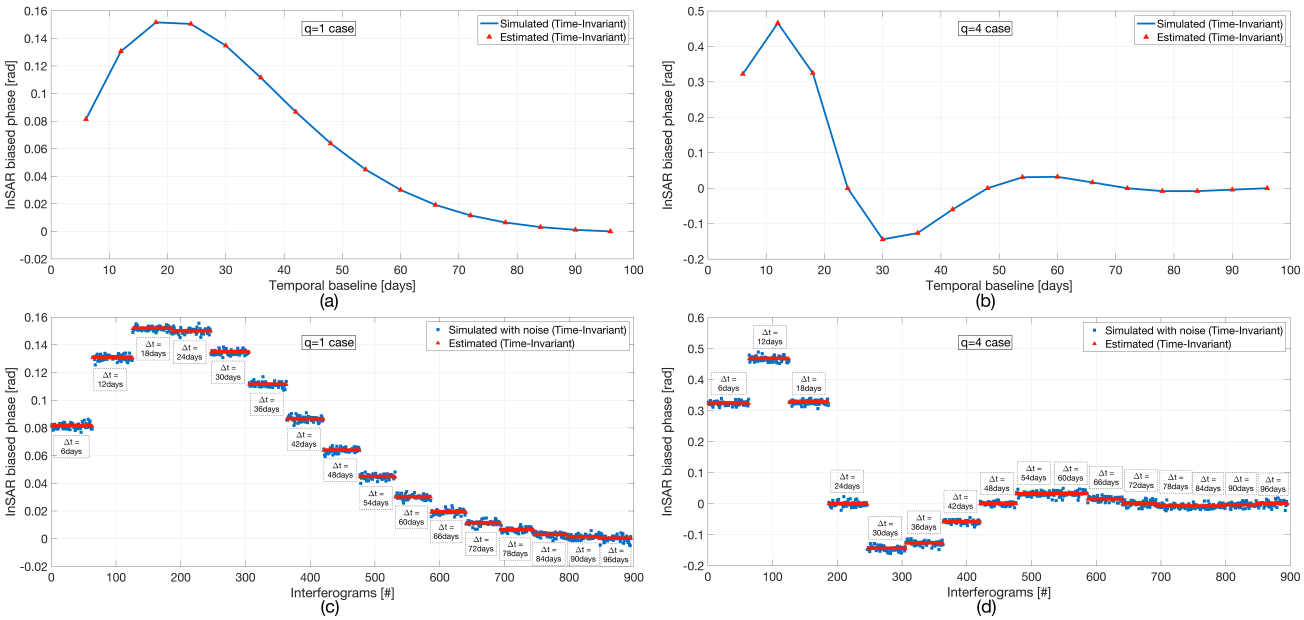

Fig. 5. Simulated and estimated InSAR biased phases for the time-invariant baseline case. (a) and (b) Noise-free simulations, where the blue lines represent the simulated phases $\Delta\phi_{h,k}^{\mathrm{ML}}$, whereas the red triangles represent the estimated phases by applying the method in Section III-A. The plots are functions of the InSAR temporal baselines. (c) and (d) Same as (a) and (b) but with noise. The plots are functions of the simulated 895 interferograms, which have been grouped and ordered by temporal baselines. (a) and (c) Simulation with $q = 1$. (b) and (d) Simulation with $q = 4$.

phases. We want to remark that, even with $q = 4$, the simulated phases do not lead to phase triplet ambiguities, that is, $\Delta\phi^{\mathrm{tr}} \in [-\pi, \pi]$. For instance, if we consider a triplet with side lengths of 6, 6, and 12 days, the excess phase $2\Delta\phi_{6\,\mathrm{days}} - \Delta\phi_{12\,\mathrm{days}}$ is of about 0.1787 rad. The same does not happen if we use for phase estimation, instead of triplets, closed loops forming polygons in the temporal/perpendicular baseline plane with several SB arcs. Indeed, if we consider a polygon formed by $A = 10$ arcs of side length 6 days and one arc of side $6A$ days, the excess phase $A\Delta\phi_{6\,\mathrm{days}} - \Delta\phi_{60\,\mathrm{days}}$ is of about 3.1909 rad, which is outside the range $[-\pi, \pi]$. In this case, the polygons must first be unwrapped, and this operation could introduce some undesired artifacts in the phase bias estimates.

The estimated phases are shown with red triangles in Fig. 5(a) and (b). The results show that when the model in (6) is time-invariant, and in the absence of noise, the method perfectly reconstructs the InSAR biased phases, also when they exhibit a sign change [see Fig. 5(b)]. Fig. 5(c) and (d) shows the results of the simulations obtained by adding to simulated phases the phase noise components $\zeta_{h,k} \neq 0$, for the two cases with $q = 1$ and 4. ML noise signals have been simulated (e.g., see the statistics shown in [48]) considering a coherence value of 0.35 and an equivalent look number (ELN) of 80. The results demonstrate that the proposed method is robust to decorrelation noise artifacts.

B. Time-Variant Case

At this stage, we study what happens in the more general case that the model (6) is time-variant, i.e., $\Delta\phi_{h,k}^{\mathrm{bias}} = \Delta\phi_{h,k}^{\mathrm{bias}}(t_h, t_k)$. To this aim, we have considered that the second family of scatterers has the following inherent phase signal $\Delta\phi_{h,k}^{\mathrm{ML},2} = \xi\,\Delta t_{h,k} + \eta_{h,k}$. Specifically, we have added to the simulated signal of Section IV-A a seasonal component for the average phase of the second family, considering a sinusoidal signal with a period of one year, $\tau = 365$ days, namely, $\eta_{h,k} = \sin[2\pi(t_k - t_0)/\tau] - \sin[2\pi(t_h - t_0)/\tau]\ \forall h, k$. As a result, the simulated phase signal is: $\Delta\varphi_{h,k}^{\mathrm{ML}} = W\{\angle[1 + e^{-\alpha\,\Delta t_{h,k}} e^{j(\xi\,\Delta t_{h,k} + \eta_{h,k})}]\}$. The phase estimation method described in Section III-B is applied in this case.

TABLE I
DETAILS OF THE TEMPORAL WINDOWS USED FOR SIMULATIONS

Temporal window [#]	Start time (t_h) [date]	End time (t_k) [date]	Temporal duration [days]
001	January 6th, 2020	January 12th, 2020	6
137	March 6th, 2020	March 18th, 2020	12
170	March 18th, 2020	April 5th, 2020	18
251	April 17th, 2020	May 11th, 2020	24
316	May 11th, 2020	June 10th, 2020	30
397	May 29th, 2020	August 3th, 2020	36

Fig. 6(a) [Fig. 6(b)] shows the plots of the estimated interferograms biased phases (biased phase velocity) versus the InSAR temporal baseline for six selected temporal windows (dashed lines), which corresponds to the InSAR data pairs listed in Table I. In this first case, we have considered $\xi = q\pi(1/\Delta t_{\max})$ with $q = 1$. The same has been repeated considering $q = 4$. The plots of the estimated biased phases (biased velocity phases) versus the InSAR temporal baselines are shown in Fig. 6(c) [Fig. 6(d)]. Black solid lines in the plots of Fig. 6 represent the estimated phases retrieved using

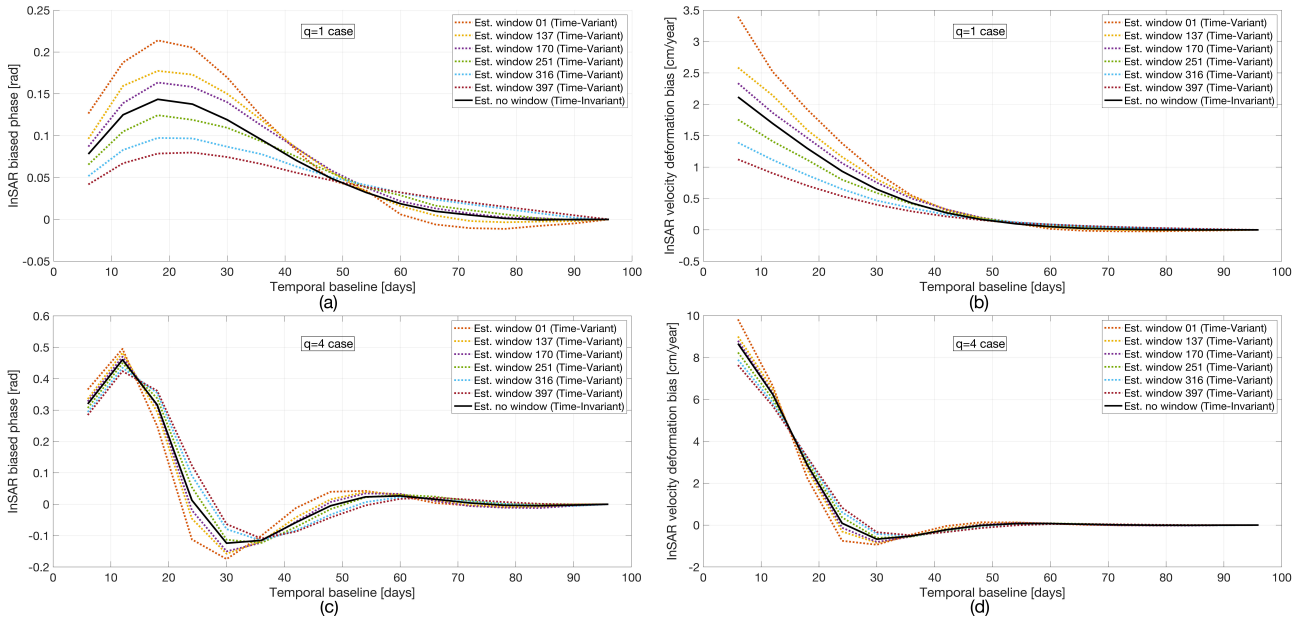

Fig. 6. (a) and (c) Estimated InSAR phases biases, and (b) and (d) the same as (a) and (c) but expressed in terms of phase velocity biases for the simulated time-variant case. The black solid lines represent the estimates when the time-invariant method (see Section III-A) is applied, whereas the dashed lines represent the time-variant estimates, for some selected temporal windows, by applying the time-variant methods presented in Section III-B. The plots are the function of the InSAR temporal baselines. (a) Simulation for the case with $q = 1$. (b) As (a) but expressed in terms of phase velocity bias. (c) Simulation for the case with $q = 4$. (d) As (c) but expressed in terms of phase velocity bias.

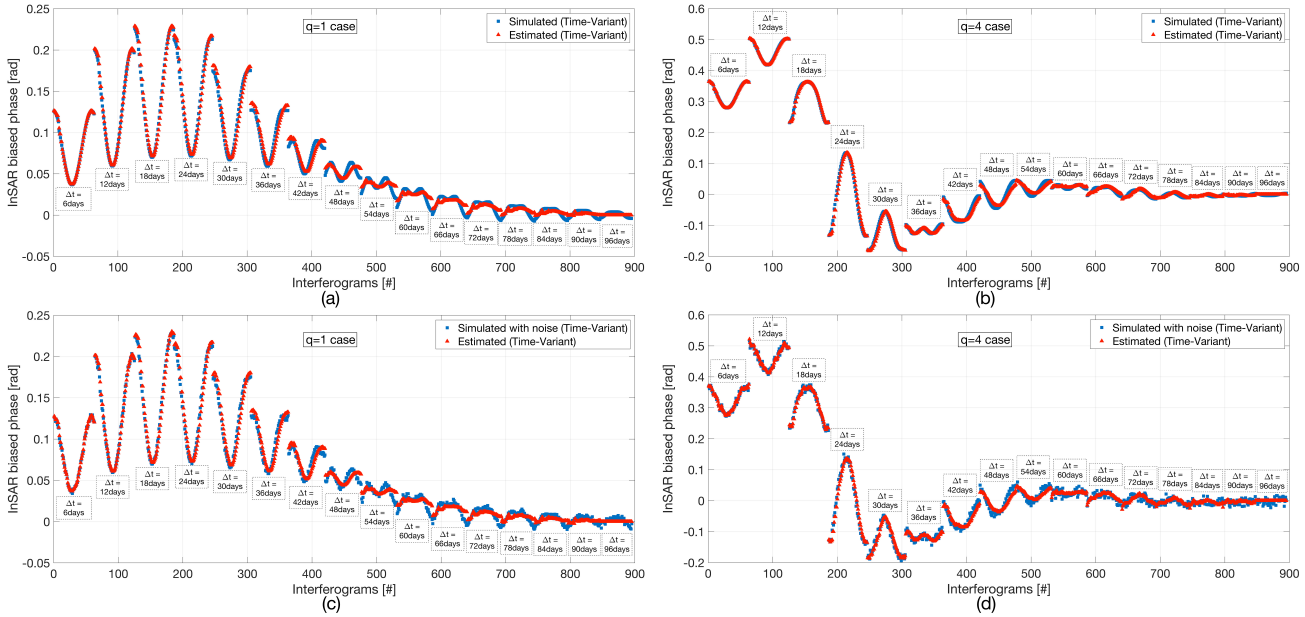

Fig. 7. Simulated and estimated InSAR biased phases for the time-variant baseline case. The blue squares represent the simulated InSAR biased phases, while the red triangles represent the estimated InSAR biased phases by applying the temporal variant baseline method in Section III-B. The simulated 895 interferograms have been grouped and ordered by temporal baselines. (a) and (b) Noise-free simulations. (c) and (d) With noise. Simulation for (a) and (c) $q = 1$ case, and (b) and (d) $q = 4$ case.

the time-invariant algorithm of Section III-A. We can observe that the time-invariant method cannot follow the time-variant fluctuations of the adopted model. Fig. 7(a) and (b) shows the comparison between the simulated and the estimated biased phases for both the scenarios with $\xi = q\pi\,(1/\Delta t_{\max})$ using $q = 1$ and 4. Simulated biased phases (blue squares) accounting for the time-variant $\eta_{h,k}$ terms have been shown as well as the relevant estimates (red triangles) obtained by applying the method described in Section III-B. The achieved results evidence that the biased phases have correctly been estimated using the developed method, which can track the different fluctuations of the phase bias in the interferograms that belong to every group of temporal baselines, especially for those with small and very small baselines. Also, in this case, we have evaluated the effects of the noise on the phase estimates. The results are shown in Fig. 7(c) and (d).

V. SB MT-INSAR METHODS

In this work, we refer to a unified representation of the SB algorithms. Indeed, the different implementations of the SB methods proposed in the literature have individual peculiarities; however, they can almost be unified [47], [66] considering that they solve a linear optimization problem that relates the vector of the (known) unwrapped ML SB interferograms, namely, $\Delta\mathbf{\Phi} = [\Delta\phi_0, \Delta\phi_1, \ldots, \Delta\phi_{M-1}]^T$, to a model of Q unknown parameters of the ground deformation $\mathbf{M}_d = [M_{d,0}, M_{d,1}, \ldots, M_{d,Q-1}]^T$. The adopted unified representation of the SB linear transformation is given as follows:

$$\mathbf{B} \cdot \mathbf{M}_d = \Delta\mathbf{\Phi} \tag{18}$$

where $\mathbf{B} \in \mathbb{R}^{M\times Q}$ is the design matrix of the considered linear transformation. Precisely, for the implementation of the Small-BAseline Subset (SBAS) algorithm [18], the model parameters represent the velocities between time-consecutive SAR acquisitions, namely, $\mathbf{M}_d = \mathbf{v} = [v_0 = ((\phi_1 - \phi_0)/(t_1 - t_0)), v_1 = ((\phi_2 - \phi_1)/(t_2 - t_1)), \ldots, v_{N-2} = ((\phi_{N-1} - \phi_{N-2})/(t_{N-1} - t_{N-2}))]^T$, and the mathematical expression of the design matrix $\mathbf{B}$ is that detailed in [18] and [66]. Once (18) is solved, the obtained model vector $\hat{\mathbf{v}}$ is time-conservative, that is to say, there exists a unique vector $\hat{\mathbf{\Phi}}$ that satisfies the following relation $\mathbf{B} \cdot \hat{\mathbf{v}} = \mathbf{A} \cdot \hat{\mathbf{\Phi}}$ and the Euclidean two-norm $\|\mathbf{A} \cdot \hat{\mathbf{\Phi}} - \Delta\mathbf{\Phi}\|_2$ is minimal, where $\mathbf{A}$ is the incidence matrix of the SB network nonplanar graph (which is equivalent to the discrete gradient operator) and $\hat{\mathbf{\Phi}}$ is the vector of the (unwrapped) phases associated with every single SAR image [66]. Here, we explicitly address some critical properties of the vector $\Delta\mathbf{\Phi}$. First, we observe that the mth (wrapped) phase $\Delta\varphi_m$ can be decomposed into the sum of a time-consistent $\Delta\varphi'_m$ and a time-inconsistent $\Delta\varphi''_m$ phase component [67]. Therefore,

$$\Delta\phi_m = \Delta\varphi'_m + \Delta\varphi''_m + 2\pi U_m, \quad m = 0, 1, \ldots, M-1 \tag{19}$$

where U_m is the correct (unknown) ambiguity number associated with the mth ML interferogram, which also considers the ambiguity number that could arise from the sum of the wrapped phase terms $\Delta\varphi'_m + \Delta\varphi''_m$. Of great relevance for the generation of the ground displacement products through SB methods are the time-inconsistent phase terms $\Delta\phi''_m$, which (as said) are responsible for nonclosure phase triplets (see Section III). This section shows how the residuals of the LS solution of (18), namely, $\Delta\mathbf{\Phi}^{\text{res}} = \mathbf{B} \cdot \hat{\mathbf{M}}_d - \Delta\mathbf{\Phi}$, are related to the nonclosure phase triplets. Moreover, we summarize some basic properties of the temporal coherence quality factor [22] to provide a quantitative estimate of the PhU errors committed after the SBAS inversion [3], [18], [22], [68]. We can express it as

$$\Gamma_{\text{temp}} = \frac{1}{M}\left|\sum_{m=0}^{M-1} \exp\left[j\,\Delta\phi_m^{\text{res}}\right]\right| \in [0, 1] \tag{20}$$

where $\Delta\phi_m^{\text{res}}$ is the mth element of the residual vector $\Delta\mathbf{\Phi}^{\text{res}} = (\mathbf{B} \cdot \hat{\mathbf{M}}_d - \Delta\mathbf{\Phi}) \in \mathbb{R}^M$. Accordingly, the temporal coherence Γ_{temp} is the mean resultant length of the circular phase data vector $\Delta\mathbf{\Phi}^{\text{res}}$. We can observe that

$$\mathbf{\Omega} \cdot \Delta\mathbf{\Phi}^{\text{res}} = \mathbf{\Omega} \cdot \left(\mathbf{A} \cdot \hat{\mathbf{\Phi}} - \Delta\mathbf{\Phi}\right) \tag{21}$$

where $\mathbf{\Omega} \in \mathbb{Z}^{\Lambda\times M}$ is the discrete curl operator related to the SB network graph, which is a sparse matrix composed of Λ (number of triplets) rows and M (number of interferograms) columns. Considering (19), (21) can be manipulated as follows:

$$\mathbf{\Omega} \cdot \Delta\mathbf{\Phi}^{\text{res}} = \mathbf{\Omega} \cdot \mathbf{A} \cdot \hat{\mathbf{\Phi}} - \mathbf{\Omega} \cdot \left[\Delta\mathbf{\Phi}' + \Delta\mathbf{\Phi}'' + 2\pi\hat{\boldsymbol{U}}\right] \tag{22}$$

where $\hat{\boldsymbol{U}} \neq \boldsymbol{U}$ is the vector of ambiguity numbers estimated through PhU operations, which could generally differ from the correct (unknown) vector $\boldsymbol{U}$. Note also that $\mathbf{\Omega} \cdot \mathbf{A} \cdot \hat{\mathbf{\Phi}} = \mathbf{0}$ and $\mathbf{\Omega} \cdot \Delta\mathbf{\Phi}' = \mathbf{0}$ being the former the discrete counterpart of the $\nabla \times \nabla\mathbf{\Phi}$ operator and $\Delta\mathbf{\Phi}'$ a time-conservative vector. Furthermore, if the estimated ambiguity number vector is not correct, namely, $\hat{\boldsymbol{U}} = \boldsymbol{U} + \Delta\boldsymbol{U}' + \Delta\boldsymbol{U}''$, where $\Delta\boldsymbol{U}'$ and $\Delta\boldsymbol{U}''$, respectively, are the time-correlated and time-uncorrelated ambiguity number errors, the following relation holds:

$$\mathbf{\Omega} \cdot 2\pi\hat{\boldsymbol{U}} = \mathbf{\Omega} \cdot 2\pi\left(\boldsymbol{U} + \Delta\boldsymbol{U}' + \Delta\boldsymbol{U}''\right) = 2\pi\left(\mathbf{\Omega} \cdot \Delta\boldsymbol{U}''\right) \tag{23}$$

because the (true) phase ambiguity cycles and the time correlated ambiguity number errors are time-conservative, namely, $2\pi(\mathbf{\Omega} \cdot \boldsymbol{U}) = \mathbf{0}$ and $2\pi(\mathbf{\Omega} \cdot \Delta\boldsymbol{U}') = \mathbf{0}$. If we assume that no PhU errors were committed, i.e., $\Delta\boldsymbol{U}'' = \mathbf{0}$, (22) particularizes as

$$\mathbf{\Omega} \cdot \Delta\mathbf{\Phi}^{\text{res}} = -\Delta\mathbf{\Phi}^{\text{tr}} \tag{24}$$

where $\Delta\mathbf{\Phi}^{tr} = W(\mathbf{\Omega} \cdot \Delta\mathbf{\Phi}'') \in \mathbb{R}^{\Lambda}$ is the vector of temporal nonclosure phase triplets, see (3). In (24), we have also assumed that phase triplets are within $[-\pi, \pi]$. Equation (24) relates the LS residuals after SB inversion $\Delta\mathbf{\Phi}^{\text{res}}$ and the nonclosure phase triplets $\Delta\mathbf{\Phi}^{\text{tr}}$, making it evident that noncompensated phase triplets correspond to errors after the SB inversion and have an impact on the temporal coherence. Finally, if we relax the hypothesis that no PhU errors were committed, we have $\mathbf{\Omega} \cdot \Delta\mathbf{\Phi}^{\text{res}} = -\Delta\mathbf{\Phi}^{\text{tr}} - 2\pi\,\mathbf{\Omega} \cdot \Delta\boldsymbol{U}''$. Therefore, the phase residuals increase due to PhU errors and the corresponding values of the temporal coherence decrease. Note that even with a perfect compensation of the systematic and random (wrapped) nonclosure phases, some significant phase residuals could still arise after applying the SB inversion to unwrapped interferograms if substantial PhU errors are present.

VI. EXPERIMENTAL RESULTS

The experiments have been carried out by independently analyzing two sets of SAR acquisitions collected over the Monte Cristo Range area, Nevada, USA, and Sicily, Italy, respectively, composed of 65 descending Sentinel-1 A/B (C-Band) SAR images acquired with terrain observation by progressive scan (TOPSAR) mode (Path 71, vertical-vertical (VV) polarization) from 6 January 2020 to 30 January 2021, and 71 descending Sentinel-1A/B TOPSAR images (Path 124, VV polarization) acquired from 16 March 2020 to 10 May 2021.

A. Nevada, USA

The area is located in the Monte Cristo Range, approximately 38-km west-northwest of Tonopah. On 15 May 2020, a severe 6.5-Mw earthquake struck the west side of the

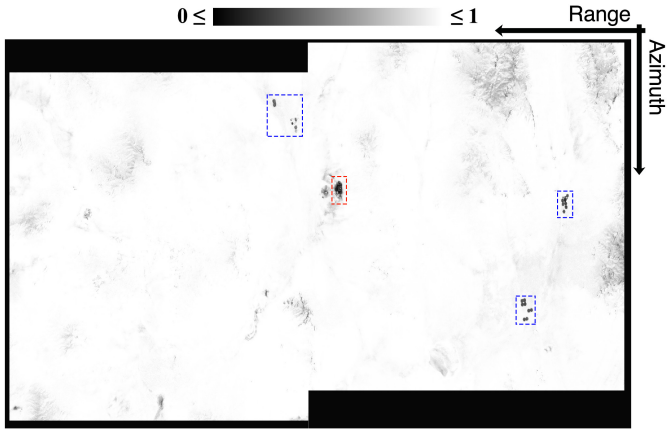

Fig. 8. Triangular coherence map of the area surrounding the Monte Cristo Range, Nevada, USA. The map has been obtained using 6305 phase triplets computed by 895 ML SB Sentinel-1 A/B interferograms. The investigated scene is almost entirely coherent, with the exception of some localized areas that are highlighted by blue and red dashed rectangles.

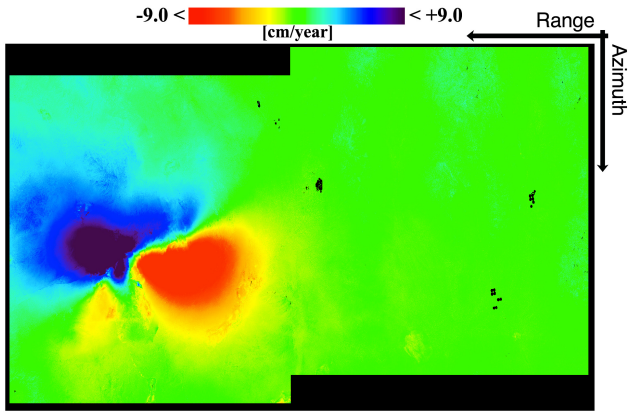

Fig. 9. Mean displacement velocity map of the area surrounding the Monte Cristo Range, Nevada, USA, computed from the interferometric network with a maximum temporal baseline threshold of 96 days and without applying any phase bias correction. The earthquake fault separates the areas in motion of uplift and subsidence. Colored pixels are all those that have a triangular coherence value greater than or equal to 0.50 and that have a final temporal coherence value greater than or equal to 0.70.

selected area, fortunately without casualties. The 2020 Monte Cristo Range earthquake represents one of the strongest earthquakes in Nevada in the past 100 years, precisely the strongest since 1954 [69]. Starting from the available SAR, ML SB interferograms were generated, by considering a temporal baseline threshold of 96 days. For the interferogram generation, we adopted an ML factor of 4 and 20 pixels for the azimuth and range directions, respectively. The one-arcsec shuttle radar topography mission (SRTM) digital elevation model (DEM) of the scene and precise orbits of the Sentinel-1 A/B satellites was used to compute the topographic phase and flatten the interferograms.

Fig. 8 shows the triangular coherence map of the investigated area, calculated considering $\Lambda = 6305$ phase triplets computed over a selected network of 895 SB ML interferograms. Subsequently, we have imposed the threshold $\gamma_{\text{triang}} = 0.50$ and exclusively processed the selected coherent pixels, which are almost three million. The phase related to the group of coherent SAR pixels was unwrapped through the minimum cost flow (MCF) solver [62], and then, the SBAS [18], [68] inversion was applied. As a result, the line-of-sight (LOS) mean displacement ground velocity map of the area was obtained, which is shown in Fig. 9, where the effects of the strong rupture ascribable to the Mw 6.5 Monte Cristo Range earthquake are evident. Indeed, on the left part of the scene, the areas straddling the fault line, showing opposite LOS deformation trends, are evidenced with an absolute value of maximum LOS mean displacement velocity of about 20 cm/year. We specify that the mean displacement velocity map, shown in Fig. 9, has been computed from the interferometric network composed of 895 ML InSAR pairs with a maximum temporal baseline of 96 days, without having applied any phase bias correction method.

Next, we have applied the phase bias estimation methods described in Sections III-A and III-B (for the time-invariant and time-variant cases) to the Nevada SAR data set using networks of SB interferograms, with a progressively reduced maximum temporal baseline (i.e., from 96 to 12 days). The selected SB ML interferograms were independently

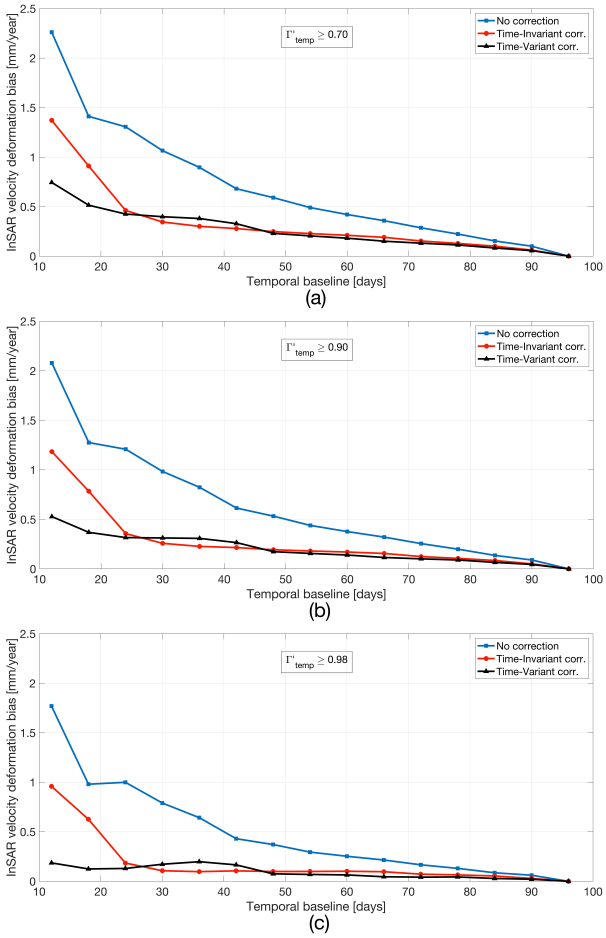

Fig. 10. Average absolute values, related to the Nevada test case, of the difference between the computed ground deformation velocities using SB networks at given temporal baseline thresholds and those achieved considering a maximum temporal baseline of 96 days. In blue, no corrections applied; in red, the time-invariant correction applied; and in black, the time-variant correction applied. Temporal coherence greater than (a) 0.7, (b) 0.9, and (c) 0.98.

corrected, unwrapped, and inverted through the SBAS technique [18]. Then, for every SAR pixel, the values of the mean ground displacement velocity and the temporal coherence have

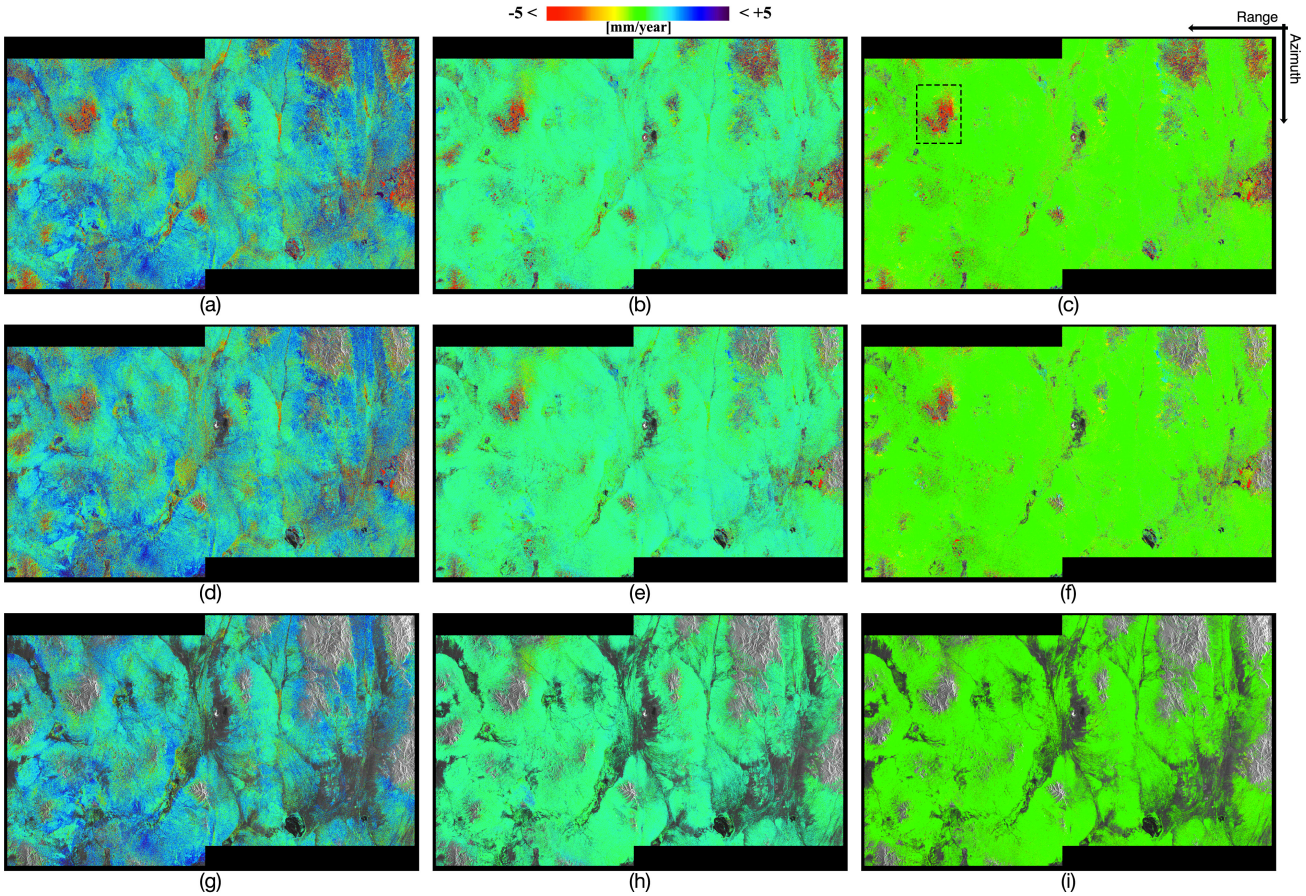

Fig. 11. Nevada test-site area maps of the ground deformation velocity differences between the case at 12 and 96 days, where only pixels larger than given values of the temporal coherence are depicted. (a), (d), and (g) Ground deformation velocity bias considering the original interferograms. (b), (e), and (h) Ground deformation velocity bias when the time-invariant correction method is applied. (c), (f), and (i) Ground deformation velocity bias when the time-variant correction method is applied. Temporal coherence greater than (a)–(c) 0.7, (d)–(f) 0.9, and (g)–(i) 0.98.

been computed. Note that, for the subsequent analyses, the atmospheric phase screen (APS) and the residual topography components were not compensated for. Fig. 10 shows the plot of the (average) absolute values of the difference between the computed ground deformation velocities using SB networks at given temporal baseline thresholds with respect to those achieved by considering as a reference a maximum temporal baseline of 96 days. Three groups of coherent SAR pixels have been identified with temporal coherence values greater than 0.7 in Fig. 10(a), 0.90 in Fig. 10(b), and 0.98 in Fig. 10(c). For every group, we plotted the absolute velocity biases (mm/year) for the original ML interferograms (blue line), the ML interferograms compensated using the time-invariant phase bias estimation method (red line), and those compensated with the time-variant method (black line). The results show that with high temporal coherence values, the developed phase bias estimation methods reveal effective, and the time-variant algorithm has a better performance than the time-invariant one, especially at very SBs. Both the phase bias estimation methods can reduce the effects of the ground displacement velocity biases of the ML interferograms with respect to what happens using the original, uncompensated interferograms. Fig. 11 shows the maps of the ground deformation velocity differences between the results at temporal baselines of 12 and 96 days, where only pixels larger than the given values of the

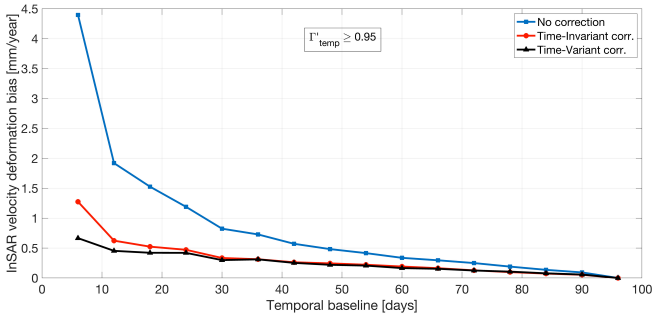

Fig. 12. Average absolute values, related to the Sicily Island test case, of the difference between the computed ground deformation velocities using SB networks at given temporal baseline thresholds with respect to those achieved considering a maximum temporal baseline of 96 days. No correction (blue), time-invariant correction (red), and the time-variant correction (black). Temporal coherence is greater than 0.95.

temporal coherence are mapped. More specifically, Fig. 11(a)–(c) shows the ground deformation velocity bias map for the original interferograms, those compensated using the time-invariant phase bias estimation method, and finally those obtained using the time-variant ones, respectively. The maps portray only SAR pixels with temporal coherence values larger than 0.7. Fig. 11(d)–(f) is the same as in Fig. 11(a)–(c) but shows only SAR pixels

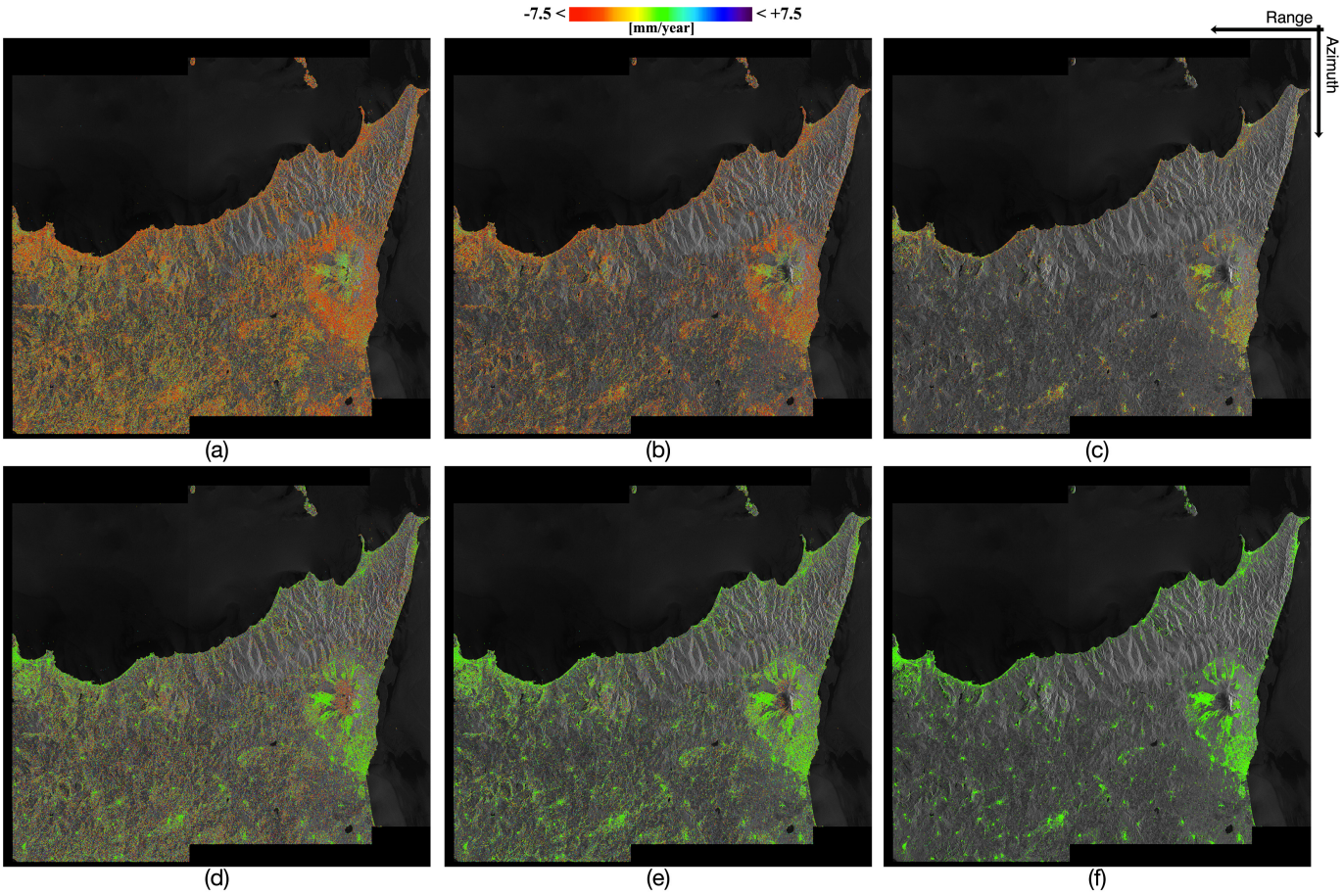

Fig. 13. Sicily Island test area maps of the ground deformation velocity differences between the results at temporal baselines of 6 and 96 days, where only pixels larger than given values of the temporal coherence are mapped. (a)–(c) Velocity bias considering original interferograms. (d)–(f) Velocity bias when the time-variant phase bias correction method is applied. Temporal coherence greater than (a) and (d) 0.5, (b) and (e) 0.7, and (c) and (f) 0.95.

with a temporal coherence larger than 0.9, and Fig. 11(g)–(i) shows only those with a temporal coherence larger than 0.98. As demonstrated in Section V, the temporal coherence is sensitive both to time-inconsistent phase terms and PhU errors. No substantial ground deformation velocity biases can be appreciated in the maps of Fig. 11(i) as well as in the relevant plot (black line) of Fig. 10(c), whereas with the same temporal coherence threshold, they were evident. This demonstrates that the developed methods are effective. The areas with lower temporal coherence values are more affected by time-inconsistent PhU errors and the latter can be responsible for some of the observed ground deformation velocity differences, see, for instance, the area highlighted by the black rectangle (dashed line) in Fig. 11(c).

B. Sicily, Italy

As a second case study, we have considered a dataset of Sentinel-1 SAR data gathered over the area of Sicily, Italy. The investigated area is home to one of the most important active volcanoes of the world, the Mount Etna volcano, which has been continuously active for the last three decades. Several InSAR investigations have been carried out in recent years for the characterization of the magmatic sources beneath the volcano cones and for the study of the superficial effects of volcanic eruptions and relevant local seismicity [42], [70], [71]. First, starting from the available SAR images, we have generated 1000 SB ML interferograms with a maximum temporal baseline of 96 days. The interferograms were flattened using a three-arcsec DEM of the Sicily Island and precise orbital information. The interferograms were multilooked with a box of 4 $\times$ 20 (azimuth and range) SAR pixels and unwrapped [62]. We have identified different networks of SB InSAR data pairs by imposing progressively decreased maximum temporal baseline thresholds, from 96 to 6 days, and we cross-compared the values of the ground displacement velocities taking as a reference the results achieved using a maximum InSAR temporal baseline of 96 days. Also, in this case, to exclude their effects on the cross-comparison analysis of the InSAR products, we did not filter out the APS and the residual topographic components from the generated InSAR products. It is worth remarking that in practical cases, other strategies could also be used to identify subsets of SB ML interferograms and use them to generate the ground displacement products [3], [54], [72]. In this work, we want to emphasize the performance of the developed methods in the general case that conventional ML SB interferograms are used, which are straightforwardly selected by imposing a threshold on their maximum allowed temporal baseline.

Fig. 12 shows the plot of the (absolute) SBAS-driven ground displacement velocity differences versus the maximum temporal baseline of the used network of SB interferograms, taken as a reference the ground displacement velocity obtained using 96 days as the maximum temporal baseline. The three plots are related to the original interferograms (blue line), the interferograms compensated using a time-invariant model (red line), and those obtained considering a time-variant model (black line). To exclude that (at most) the ground deformation velocities difference could be due to time-inconsistent PhU errors,[3] only SAR pixels with a very high value of the temporal coherence (i.e., larger than 0.95) have been considered. The results show that the developed phase bias estimation methods are capable of considerably reducing the effects related to systematic phase biases in the generated ground displacement maps. Note that in this case, we have also considered the extreme case when only six-day interferograms are used to compute the ground displacement time-series. We want to remark that any potential PhU error on such six-day interferograms has a severe impact because it is time-integrated and appears as an undesired jump in the obtained ground deformation time-series. Fig. 13 shows the maps of mean displacement velocity differences between the results obtained from 96 to 6 days, for the original one in Fig. 13(a)–(c), and those corrected by applying the developed phase estimate time-variant method in Fig. 13(d)–(f). The maps are obtained by considering different temporal coherence thresholds to make it evident the spatial distribution of SAR pixels that are more affected by PhU errors.

VII. Conclusion

The properties of nonclosure phase triplets in sequences of ML SB interferograms have been addressed in this research study. We have shown that phase triplets and phase residuals, arising from the LS inversion of the unwrapped SB interferograms, are linked to one another. We have discussed the implications of ML nonclosure phase triplets on the claimed fading signals [34] into the SB-driven mean ground displacement maps obtained using very SB SAR interferograms. Two methods that could be adopted to reduce the effects of noncompensated systematic phase biases in the generated ground displacement time series have been proposed, considering both a time-invariant and time-variant model for the systematic phase bias signals. The results obtained by applying the developed algorithms to simulated and real SAR data have also been presented and discussed. The methods rely on the exclusive use of triplets of ML interferograms, instead of using polygons of ML SB interferograms, and assume that the systematic phase bias rapidly decays over time, and it is negligible at large temporal baselines. We also proposed a recursive strategy to understand at which temporal baseline we could reasonably assume that the phase bias is almost zero. It consists of adding long-baseline ML interferograms that are, however, only used to implement the phase bias correction step, and they are subsequently discarded for the generation of ground displacement time series. Yet, we have shown that nonclosure phase triplets can be used to effectively identify a group of coherent SAR pixels at the ML scale over which ground deformation InSAR products can be computed.

Globally, our research study demonstrates that, under proper hypotheses, with the preliminarily compensation/reduction of the systematic phase errors in the sequence of original wrapped interferograms, the SB Mt-InSAR methods reveal effective for the generation of ground displacement products, also with new-generation SAR systems characterized by frequent repetition times (on a weekly basis or less). Nevertheless, further developments are still required to understand the ultimate consequences of the very small baselines and nonclosure phase triplets for the detection and analysis of soil properties and other "hidden" signals that can be extracted from sequences of SB ML InSAR interferograms.

As a final remark, we want to highlight that for the presented investigations, we have intentionally not used 3-D [73], [74], [75] or hybrid 2-D + 2-D PhU methods [22], [26], [28]. Conversely, we have unwrapped every single interferogram independently [62]. Also, we have selected the SB interferograms to be inverted by simply imposing a threshold on the maximum allowed temporal baseline of the interferograms. We followed this strategy precisely to emphasize the role played by the systematic phase artifacts and PhU errors.

Appendix I

Let us consider the Λ_χ-length random directional data vector $[\varphi^{\mathrm{tr}}_{\chi_0}, \varphi^{\mathrm{tr}}_{\chi_1}, \ldots, \varphi^{\mathrm{tr}}_{\chi_{\Lambda_\chi-1}}]^T$ which are assumed to be Von-Mises distributed $\mathrm{VM}(\mu_\chi, \kappa_\chi)$. From the work [56], we can consider its resultant vector, which is the following random variable:

$$S = \frac{1}{\Lambda_\chi}\sum_{z=0}^{\Lambda_\chi-1}\exp\left(j\varphi^{\mathrm{tr}}_{\chi_z}\right) = R_\chi \exp\left(j\Phi_\chi\right) \tag{I.1}$$

where R_χ and Φ_χ are the mean resultant length and the mean direction of the considered directional data vector, respectively. Let us also ρ_χ and μ_χ assume be the average (sampled) values of the mean resultant length and the mean direction, respectively.

For large samples, e.g., $\Lambda_\chi \gg 1$, it can be shown [56] that the following relations hold:

$$\Lambda_\chi \mathrm{var}\left(R_\chi\right) \cong \frac{\rho_\chi^2\left(1-2\rho_\chi^2\right)+\alpha_2\left(\alpha^2-\beta^2\right)2\alpha^2+2\alpha\beta\beta_2}{2\rho_\chi^2} \tag{I.2}$$

$$\Lambda_\chi \mathrm{var}\left(\Phi_\chi\right) \cong \frac{\rho_\chi^2+\alpha_2\left(\alpha^2-\beta^2\right)2\alpha^2-2\alpha\beta\beta_2}{2\rho_\chi^4} \tag{I.3}$$

where $\alpha = E[\sum_{z=0}^{\Lambda_\chi-1}\cos(\varphi^{\mathrm{tr}}_{\chi_z})/\Lambda_\chi]$, $\alpha_2 = E[\sum_{z=0}^{\Lambda_\chi-1}\cos(2\varphi^{\mathrm{tr}}_{\chi_z})/\Lambda_\chi]$, $\beta = E[\sum_{z=0}^{\Lambda_\chi-1}\sin(\varphi^{\mathrm{tr}}_{\chi_z})/\Lambda_\chi]$, and $\beta_2 = E[\sum_{z=0}^{\Lambda_\chi-1}\sin(2\varphi^{\mathrm{tr}}_{\chi_z})/\Lambda_\chi]$.

[3]Note that time-inconsistent PhU errors are not present when pure 3-D PhU methods [73], [74], [75] are used, but, conversely, PhU errors could still be present and be totally indistinguishable from the true ground deformation signal. On the other hand, hybrid 2-D + 2-D PhU methods [22], [26], [28] and conventional 2-D PhU methods [62], [63], [64], [65] can make it evident time-inconsistent PhU errors and the temporal coherence can be used to check them and neglect those pixels that are severely affected by them.

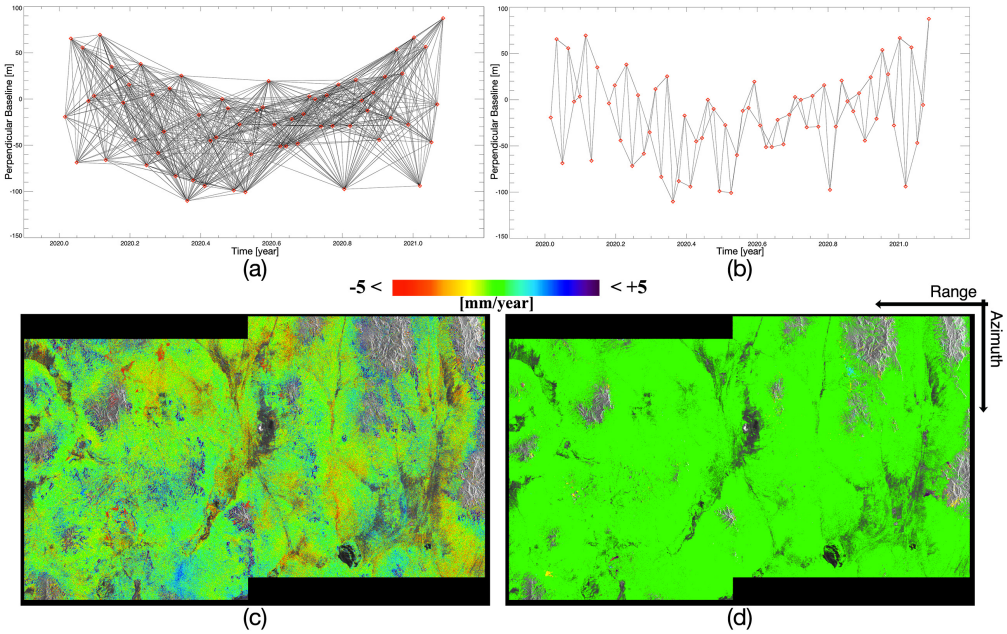

Fig. 14. (a) Distribution of the SB interferometric SAR data pairs for the Nevada case-study area as obtained by imposing a maximum temporal baseline of 96 days. (b) Distribution of the SB interferometric SAR data pairs for the Nevada case-study area as obtained by imposing a maximum temporal baseline of 12 days. (c) Difference between the mean ground deformation velocity of the area obtained by independently applying the E-Mt-InSAR noise-filtering method [57] and the SBAS inversion [18] to the SB networks depicted in (a) and (b). (d) Difference between the mean ground deformation velocity of the area obtained by independently applying only the E-Mt-InSAR algorithm in the network (a), and subsequently, the noise-filtered interferograms (a) or a subset of them (b) are inverted through the SBAS algorithm and obtain the results at (a) 96 days and (b) 12 days.

Interested readers can find some approximate relationships for the variance of Φ_χ and R_χ in [56, pp. 76–78]. For instance, the variance of the phase is better described with

$$\Lambda_\chi \mathrm{var}(\Phi_\chi) \cong \frac{1}{\kappa_\chi}\left[1+\frac{1}{2\kappa_\chi}\right] \tag{I.4}$$

where κ_χ is the concentration parameter of the Von Mises distribution. Equations (I.2)–(I.4) show that the precision of the mean direction and mean resultant length measurement critically depends on the number of elements constituting the directional data vector population Λ_χ.

Appendix II

In this section, we show some experimental results obtained by applying the E-Mt-InSAR algorithm to conventional (nonphase-bias-corrected) ML interferograms. The method is detailed in [57]. Here, we want to point out that, for every analyzed SAR pixel, the optimized set of phases associated with the available N SAR acquisitions are exploited to reconstruct the set of M optimized, wholly time-consistent ML SB interferograms, namely, $\{\Delta\phi^{\mathrm{ML}}_{opt,i}\}_{i=0}^{M-1}$, which markedly have a zero phase closure.[4] Accordingly, once the E-Mt-InSAR noise-filtering method is applied, any subset of the optimized ML SB interferograms that could be extracted from $\{\Delta\phi^{\mathrm{ML}}_{opt,i}\}_{i=0}^{M-1}$ and that involves all the available N SAR acquisitions is, by design, time-consistent. Therefore, the ground deformation time series that one could generate by inverting these subsets of optimized ML SB interferograms using any SB-oriented Mt-InSAR method [18], [19], [20], [47], [54] are necessarily coincident. Of course, this statement is true when we exclude the effects of localized PhU errors and the role of some specific processing stages, such as those for the estimation of the residual topographic phase components and the compensation of the APS, whose results could depend on the selected subset of the optimized ML SB interferograms. Although the ground deformation time series obtained by inverting these different subsets of M' optimized interferograms extracted from $\{\Delta\phi^{\mathrm{ML}}_{opt,i}\}_{i=0}^{M-1}$ are coincident, however, this does not mean that the E-Mt-InSAR noise-filtering method [57] is capable of wholly compensating for the effects of the systematic phase biases in the ground displacement InSAR products, which could still be present even with coincident time series if the phase bias compensation was made incorrectly.

To prove the validity of these statements, we performed an experiment using the conventional SB ML interferograms related to the Nevada case-study area. We independently applied the E-Mt-InSAR noise-filtering method [57] to the set of SB interferograms selected with a maximum temporal baseline of 96 days [see Fig. 14(a)] and 12 days [see Fig. 14(b)]. The optimized noise-filtered interferograms were independently unwrapped [62] and inverted by the SBAS algorithm [18]. Fig. 14(c) shows the difference of the mean ground displacement velocity of the study area as obtained using the SB networks with maximum temporal baselines of 12 days [see Fig. 14(a)] and 96 days [see Fig. 14(b)].

[4]Note that the E-Mt-InSAR noise-filtering method also involves a subsequent nonlinear combination step between the original interferograms and those reconstructed from the optimized set of acquisition phase. It was proposed in [3, eq. (4)] to preserve the spatial coherence of the very coherent interferograms. This nonlinear operation, however, reintroduces some nonclosure phase triplets.

The map only depicts SAR pixels with temporal coherence values greater than 0.95 to exclude that some of the observed differences could be ascribed to PhU errors.

The achieved results show that some differences in the ground displacement velocity maps persist. As a matter of fact, the E-Mt-InSAR method [57] was designed to mitigate the decorrelation noise in sequences of ML interferograms by exploiting their temporal relationships, but it did not consider specifically the presence of short-lived systematic phase contributions that, as said, occur at small/very-small temporal baselines. Nonetheless, depending on the used network of SB interferograms, the E-Mt-InSAR method allows obtaining time-consistent filtered ML interferograms that are characterized by perfectly compensated phase closures. We also remark that the method does not require that the SB interferograms form a planar triangulation in the temporal/perpendicular baseline plane.[5]

To further prove the validity of the above-mentioned statements, we have carried out a second experiment. We have applied the E-Mt-InSAR algorithm to the network of SB interferograms shown in Fig. 14(a), characterized by a temporal baseline threshold of 96 days. Subsequently, from the generated group of 895 filtered interferograms, we have extracted a subset of them consisting of 125 filtered interferograms that form the SB network shown in Fig. 14(b) with a maximum temporal baseline of 12 days. The two sets of interferograms were unwrapped and the relevant ground displacement velocity maps were compared. Fig. 14(d) shows the mean ground deformation velocity difference between the results obtained with the SB networks at 96 days in Fig. 14(a) and 12 days in Fig. 14(b) but using for both the same set of optimized noise-filtered ML interferograms, as above clarified. The results show that the ground displacement velocity difference is almost zero everywhere but some localized zones with tiny PhU errors. Also, in this case, we only portray SAR pixels with temporal coherence values larger than 0.95. As said, this outcome does not automatically mean that the systematic phase contributions were perfectly compensated for. Conversely, it does mean that these phase artifacts cannot be easily discriminated by the (true) ground deformation signals because they are time-consistent and, hence, they do not lead to time discrepancies that could be straightforwardly visible by comparing the obtained ground displacement velocity maps.

We hope that the results of our analyses could be useful to unravel some of the (potential) reasons that are behind the apparent disagreement existing between the main outcomes of the investigations presented in [34] and [76].

ACKNOWLEDGMENT

The authors are grateful to the anonymous reviewers for their valuable comments and suggestions.

[5]We want to explicitly remark that the E-Mt-InSAR method, which is also implemented in the P-SBAS processing chain [68], [76], operates on the whole set of the selected ML SB interferograms. Only once the optimized set of noise-filtered SB ML interferograms is computed, the EMCF-based SBAS processing chain [3] exploits triangulations, but with the exclusive aim to speed up and improve the PhU operations and efficiently generate the SBAS ground displacement time series. In this work, we only applied the E-Mt-InSAR noise-filtering algorithm.

REFERENCES

[1] A. Ferretti, A. Fumagalli, F. Novali, C. Prati, F. Rocca, and A. Rucci, "A new algorithm for processing interferometric data-stacks: SqueeSAR," *IEEE Trans. Geosci. Remote Sens.*, vol. 49, no. 9, pp. 3460–3470, Sep. 2011, doi: 10.1109/TGRS.2011.2124465.

[2] F. De Zan, M. Zonno, and P. Lopez-Dekker, "Phase inconsistencies and multiple scattering in SAR interferometry," *IEEE Trans. Geosci. Remote Sens.*, vol. 53, no. 12, pp. 6608–6616, Dec. 2015, doi: 10.1109/TGRS.2015.2444431.

[3] A. Pepe, Y. Yang, M. Manzo, and R. Lanari, "Improved EMCF-SBAS processing chain based on advanced techniques for the noise-filtering and selection of small baseline multi-look DInSAR interferograms," *IEEE Trans. Geosci. Remote Sens.*, vol. 53, no. 8, pp. 4394–4417, Aug. 2015, doi: 10.1109/TGRS.2015.2396875.

[4] N. Cao, H. Lee, and H. C. Jung, "Mathematical framework for phase-triangulation algorithms in distributed-scatterer interferometry," *IEEE Geosci. Remote Sens. Lett.*, vol. 12, no. 9, pp. 1838–1842, Sep. 2015, doi: 10.1109/LGRS.2015.2430752.

[5] R. M. Goldstein and C. L. Werner, "Radar interferogram filtering for geophysical applications," *Geophys. Res. Lett.*, vol. 25, no. 21, pp. 4035–4038, Nov. 1998, doi: 10.1029/1998GL900033.

[6] I. Baran, M. P. Stewart, B. M. Kampes, Z. Perski, and P. Lilly, "A modification to the Goldstein radar interferogram filter," *IEEE Trans. Geosci. Remote Sens.*, vol. 41, no. 9, pp. 2114–2118, Sep. 2003, doi: 10.1109/TGRS.2003.817212.

[7] Z. W. Li, X. L. Ding, C. Huang, J. J. Zhu, and Y. L. Chen, "Improved filtering parameter determination for the Goldstein radar interferogram filter," *ISPRS J. Photogramm. Remote Sens.*, vol. 63, no. 6, pp. 621–634, Nov. 2008, doi: 10.1016/j.isprsjprs.2008.03.001.

[8] R. J. Michaelides, H. A. Zebker, and Y. Zheng, "An algorithm for estimating and correcting decorrelation phase from InSAR data using closure phase triplets," *IEEE Trans. Geosci. Remote Sens.*, vol. 57, no. 12, pp. 10390–10397, Dec. 2019, doi: 10.1109/TGRS.2019.2934362.

[9] F. De Zan, A. Parizzi, P. Prats-Iraola, and P. López-Dekker, "A SAR interferometric model for soil moisture," *IEEE Trans. Geosci. Remote Sens.*, vol. 52, no. 1, pp. 418–425, Jan. 2014, doi: 10.1109/TGRS.2013.2241069.

[10] S. Zwieback, S. Hensley, and I. Hajnsek, "Assessment of soil moisture effects on L-band radar interferometry," *Remote Sens. Environ.*, vol. 164, pp. 77–89, Sep. 2015, doi: 10.1016/j.rse.2015.04.012.

[11] S. Zwieback, S. Hensley, and I. Hajnsek, "Soil moisture estimation using differential radar interferometry: Toward separating soil moisture and displacements," *IEEE Trans. Geosci. Remote Sens.*, vol. 55, no. 9, pp. 5069–5083, Sep. 2017, doi: 10.1109/TGRS.2017.2702099.

[12] G. Gomba and F. De Zan, "Estimating soil moisture from SAR interferometry with closure phases," in *Proc. IEEE Int. Geosci. Remote Sens. Symp.*, Jul. 2019, pp. 6983–6985, doi: 10.1109/IGARSS.2019.8898546.

[13] Y. Eshqi Molan and Z. Lu, "Can InSAR coherence and closure phase be used to estimate soil moisture changes?" *Remote Sens.*, vol. 12, no. 9, p. 1511, May 2020, doi: 10.3390/rs12091511.

[14] Y. Eshqi Molan and Z. Lu, "Modeling InSAR phase and SAR intensity changes induced by soil moisture," *IEEE Trans. Geosci. Remote Sens.*, vol. 58, no. 7, pp. 4967–4975, Jul. 2020, doi: 10.1109/TGRS.2020.2970841.

[15] R. Michaelides and H. Zebker, "Feasibility of retrieving soil moisture from InSAR decorrelation phase and closure phase," in *Proc. IEEE Int. Geosci. Remote Sens. Symp.*, Sep. 2020, pp. 12–15, doi: 10.1109/IGARSS39084.2020.9323833.

[16] N. C. Mira, J. Catalao, G. Nico, and P. Mateus, "Soil moisture estimation using atmospherically corrected C-band InSAR data," *IEEE Trans. Geosci. Remote Sens.*, vol. 60, pp. 1–9, 2022, doi: 10.1109/TGRS.2021.3109450.

[17] B. Barrett, E. Dwyer, and P. Whelan, "Soil moisture retrieval from active spaceborne microwave observations: An evaluation of current techniques," *Remote Sens.*, vol. 1, no. 3, pp. 210–242, Jul. 2009, doi: 10.3390/rs1030210.

[18] P. Berardino, G. Fornaro, R. Lanari, and E. Sansosti, "A new algorithm for surface deformation monitoring based on small baseline differential SAR interferograms," *IEEE Trans. Geosci. Remote Sens.*, vol. 40, no. 11, pp. 2375–2383, Nov. 2002, doi: 10.1109/TGRS.2002.803792.

[19] O. Mora, J. J. Mallorqui, and A. Broquetas, "Linear and nonlinear terrain deformation maps from a reduced set of interferometric SAR images," *IEEE Trans. Geosci. Remote Sens.*, vol. 41, no. 10, pp. 2243–2253, Oct. 2003, doi: 10.1109/TGRS.2003.814657.

[20] K. Goel and N. Adam, "A distributed scatterer interferometry approach for precision monitoring of known surface deformation phenomena," *IEEE Trans. Geosci. Remote Sens.*, vol. 52, no. 9, pp. 5454–5468, Sep. 2014, doi: 10.1109/TGRS.2013.2289370.

[21] E. A. Hetland, P. Musé, M. Simons, Y. N. Lin, P. S. Agram, and C. J. DiCaprio, "Multiscale InSAR time series (MInTS) analysis of surface deformation," *J. Geophys. Res., Solid Earth*, vol. 117, no. B2, pp. 1–17, Feb. 2012, doi: 10.1029/2011JB008731.

[22] A. Pepe and R. Lanari, "On the extension of the minimum cost flow algorithm for phase unwrapping of multitemporal differential SAR interferograms," *IEEE Trans. Geosci. Remote Sens.*, vol. 44, no. 9, pp. 2374–2383, Sep. 2006, doi: 10.1109/TGRS.2006.873207.

[23] B. Pinel-Puyssegur, C. Lasserre, A. Benoit, R. Jolivet, M.-P. Doin, and J. Champenois, "A simple phase unwrapping errors correction algorithm based on phase closure analysis," in *Proc. IEEE Int. Geosci. Remote Sens. Symp.*, Jul. 2018, pp. 2212–2215, doi: 10.1109/IGARSS.2018.8518050.

[24] A. Pepe, L. D. Euillades, M. Manunta, and R. Lanari, "New advances of the extended minimum cost flow phase unwrapping algorithm for SBAS-DInSAR analysis at full spatial resolution," *IEEE Trans. Geosci. Remote Sens.*, vol. 49, no. 10, pp. 4062–4079, Oct. 2011, doi: 10.1109/TGRS.2011.2135371.

[25] A. Benoit, B. Pinel-Puysségur, R. Jolivet, and C. Lasserre, "CorPhU: An algorithm based on phase closure for the correction of unwrapping errors in SAR interferometry," *Geophys. J. Int.*, vol. 221, no. 3, pp. 1959–1970, Jun. 2020, doi: 10.1093/gji/ggaa120.

[26] C. Esch, J. Köhler, K. Gutjahr, and W.-D. Schuh, "One-step three-dimensional phase unwrapping approach based on small baseline subset interferograms," *Remote Sens.*, vol. 12, no. 9, p. 1473, May 2020, doi: 10.3390/rs12091473.

[27] F. Liu and B. Pan, "A new 3-D minimum cost flow phase unwrapping algorithm based on closure phase," *IEEE Trans. Geosci. Remote Sens.*, vol. 58, no. 3, pp. 1857–1867, Mar. 2020, doi: 10.1109/TGRS.2019.2949926.

[28] R. Li, X. Lv, J. Yuan, and J. Yao, "A triangle-oriented spatial–temporal phase unwrapping algorithm based on irrotational constraints for time-series InSAR," *IEEE Trans. Geosci. Remote Sens.*, vol. 57, no. 12, pp. 10263–10275, Dec. 2019, doi: 10.1109/TGRS.2019.2933024.

[29] A. Pepe, "The correction of phase unwrapping errors in sequences of multi-temporal differential SAR interferograms," in *Proc. IEEE Int. Geosci. Remote Sens. Symp.*, Sep. 2020, pp. 818–821, doi: 10.1109/IGARSS39084.2020.9323768.

[30] X. Xu and D. T. Sandwell, "Toward absolute phase change recovery with InSAR: Correcting for Earth tides and phase unwrapping ambiguities," *IEEE Trans. Geosci. Remote Sens.*, vol. 58, no. 1, pp. 726–733, Jan. 2020, doi: 10.1109/TGRS.2019.2940207.

[31] Z. Yunjun, H. Fattahi, and F. Amelung, "Small baseline InSAR time series analysis: Unwrapping error correction and noise reduction," *Comput. Geosci.*, vol. 133, Dec. 2019, Art. no. 104331, doi: 10.1016/j.cageo.2019.104331.

[32] M. Manunta and Y. Muhammad, "A novel algorithm based on compressive sensing to mitigate phase unwrapping errors in multitemporal DInSAR approaches," *IEEE Trans. Geosci. Remote Sens.*, vol. 60, pp. 1–20, 2022, doi: 10.1109/TGRS.2021.3079158.

[33] Z.-F. Ma, M. Jiang, M. Khoshmanesh, and X. Cheng, "Time series phase unwrapping based on graph theory and compressed sensing," *IEEE Trans. Geosci. Remote Sens.*, vol. 60, pp. 1–12, 2022, doi: 10.1109/TGRS.2021.3066784.

[34] H. Ansari, F. De Zan, and A. Parizzi, "Study of systematic bias in measuring surface deformation with SAR interferometry," *IEEE Trans. Geosci. Remote Sens.*, vol. 59, no. 2, pp. 1285–1301, Feb. 2021, doi: 10.1109/TGRS.2020.3003421.

[35] S. Zwieback et al., "A statistical test of phase closure to detect influences on DInSAR deformation estimates besides displacements and decorrelation noise: Two case studies in high-latitude regions," *IEEE Trans. Geosci. Remote Sens.*, vol. 54, no. 9, pp. 5588–5601, Sep. 2016, doi: 10.1109/TGRS.2016.2569435.

[36] H. Ansari, F. De Zan, and A. Parizzi, "Fading signal: An overlooked error source for distributed scatterer interferometry," in *Proc. IEEE Int. Geosci. Remote Sens. Symp.*, Jul. 2021, pp. 3181–3184, doi: 10.1109/IGARSS47720.2021.9554910.

[37] Y. Maghsoudi, A. J. Hooper, T. J. Wright, M. Lazecky, and H. Ansari, "Characterizing and correcting phase biases in short-term, multi-looked interferograms," *Remote Sens. Environ.*, vol. 275, Jun. 2022, Art. no. 113022, doi: 10.1016/j.rse.2022.113022.

[38] Y. Zheng, H. Fattahi, P. Agram, M. Simons, and P. Rosen, "On closure phase and systematic bias in multilooked SAR interferometry," *IEEE Trans. Geosci. Remote Sens.*, vol. 60, pp. 1–11, 2022, doi: 10.1109/TGRS.2022.3167648.

[39] P. Blanco-Sánchez, J. J. Mallorquí, S. Duque, and D. Monells, "The coherent pixels technique (CPT): An advanced DInSAR technique for nonlinear deformation monitoring," *Pure Appl. Geophys.*, vol. 165, no. 6, pp. 1167–1193, Aug. 2008, doi: 10.1007/s00024-008-0352-6.

[40] S. Usai, "A least squares database approach for SAR interferometric data," *IEEE Trans. Geosci. Remote Sens.*, vol. 41, no. 4, pp. 753–760, Apr. 2003, doi: 10.1109/TGRS.2003.810675.

[41] M.-P. Doin et al., "Presentation of the small baseline NSBAS processing chain on a case example: The Etna deformation monitoring from 2003 to 2010 using Envisat data," in *Proc. Fringe Symp.*, Sep. 2011, pp. 3434–3437.

[42] C. D. Negro et al., "Capturing the fingerprint of Etna volcano activity in gravity and satellite radar data," *Sci. Rep.*, vol. 3, no. 1, p. 1, Oct. 2013, doi: 10.1038/srep03089.

[43] F. Falabella, C. Serio, G. Masiello, Q. Zhao, and A. Pepe, "A multi-grid InSAR technique for joint analyses at single-look and multi-look scales," *IEEE Geosci. Remote Sens. Lett.*, vol. 19, pp. 1–5, 2022, doi: 10.1109/LGRS.2021.3086271.

[44] F. De Zan, F. Rocca, A. Ferretti, P. López-Dekker, and M. Eineder, "Letters comments on 'influence of the statistical properties of phase and intensity on closure phase,'" *IEEE Trans. Geosci. Remote Sens.*, vol. 59, no. 7, pp. 6277–6278, Jul. 2020, doi: 10.1109/TGRS.2020.3021130.

[45] Y. E. Molan, Z. Lu, and J.-W. Kim, "Influence of the statistical properties of phase and intensity on closure phase," *IEEE Trans. Geosci. Remote Sens.*, vol. 58, no. 10, pp. 7346–7354, Oct. 2020, doi: 10.1109/TGRS.2020.2982062.

[46] G. Fornaro, S. Verde, D. Reale, and A. Pauciullo, "CAESAR: An approach based on covariance matrix decomposition to improve multibaseline-multitemporal interferometric SAR processing," *IEEE Trans. Geosci. Remote Sens.*, vol. 53, no. 4, pp. 2050–2065, Apr. 2015, doi: 10.1109/TGRS.2014.2352853.

[47] W. Gong, A. Thiele, S. Hinz, F. Meyer, A. Hooper, and P. Agram, "Comparison of small baseline interferometric SAR processors for estimating ground deformation," *Remote Sens.*, vol. 8, no. 4, p. 330, Apr. 2016, doi: 10.3390/rs8040330.

[48] C. Lopez-Martinez and E. Pottier, "On the extension of multidimensional speckle noise model from single-look to multilook SAR imagery," *IEEE Trans. Geosci. Remote Sens.*, vol. 45, no. 2, pp. 305–320, Feb. 2007, doi: 10.1109/TGRS.2006.887012.

[49] J. Jung, S.-H. Yun, D.-J. Kim, and M. Lavalle, "Damage-mapping algorithm based on coherence model using multitemporal polarimetric–interferometric SAR data," *IEEE Trans. Geosci. Remote Sens.*, vol. 56, no. 3, pp. 1520–1532, Mar. 2018, doi: 10.1109/TGRS.2017.2764748.

[50] R. Bamler and P. Hartl, "Synthetic aperture radar interferometry," *Inverse Problems*, vol. 14, no. 4, pp. R1–R54, Aug. 1998, doi: 10.1088/0266-5611/14/4/001.

[51] H. A. Zebker and J. Villasenor, "Decorrelation in interferometric radar echoes," *IEEE Trans. Geosci. Remote Sens.*, vol. 30, no. 5, pp. 950–959, Sep. 1992, doi: 10.1109/36.175330.

[52] S. Zwieback, S. Hensley, and I. Hajnsek, "A polarimetric first-order model of soil moisture effects on the DInSAR coherence," *Remote Sens.*, vol. 7, no. 6, pp. 7571–7596, Jun. 2015, doi: 10.3390/rs70607571.

[53] B. Rabus, H. Wehn, and M. Nolan, "The importance of soil moisture and soil structure for InSAR phase and backscatter, as determined by FDTD modeling," *IEEE Trans. Geosci. Remote Sens.*, vol. 48, no. 5, pp. 2421–2429, May 2010, doi: 10.1109/TGRS.2009.2039353.

[54] F. Falabella, C. Serio, G. Zeni, and A. Pepe, "On the use of weighted least-squares approaches for differential interferometric SAR analyses: The weighted adaptive variable-length (WAVE) technique," *Sensors*, vol. 20, no. 4, p. 1103, Feb. 2020, doi: 10.3390/s20041103.

[55] F. Falabella and A. Pepe, "A method for the correction of non-closure phase artefacts in triplets of multi-look SAR interferograms," EGU Gen. Assem., Vienna, Austria, Tech. Rep. EGU22-4919, May 2022, doi: 10.5194/egusphere-egu22-4919.

[56] K. V. Mardia and P. E. Jupp, *Directional Statistics*. Chichester, U.K.: Wiley, 2000.

[57] A. Pepe, "Theory and statistical description of the enhanced multi-temporal InSAR (E-MTInSAR) noise-filtering algorithm," *Remote Sens.*, vol. 11, no. 3, p. 363, Feb. 2019, doi: 10.3390/rs11030363.

[58] H. Ansari, F. De Zan, and R. Bamler, "Efficient phase estimation for interferogram stacks," *IEEE Trans. Geosci. Remote Sens.*, vol. 56, no. 7, pp. 4109–4125, Jul. 2018, doi: 10.1109/TGRS.2018.2826045.
[59] N. Cao, H. Lee, and H. C. Jung, "A phase-decomposition-based PSInSAR processing method," *IEEE Trans. Geosci. Remote Sens.*, vol. 54, no. 2, pp. 1074–1090, Feb. 2016, doi: 10.1109/TGRS.2015.2473818.
[60] S. Samiei-Esfahany, J. E. Martins, F. van Leijen, and R. F. Hanssen, "Phase estimation for distributed scatterers in InSAR stacks using integer least squares estimation," *IEEE Trans. Geosci. Remote Sens.*, vol. 54, no. 10, pp. 5671–5687, Oct. 2016, doi: 10.1109/TGRS.2016.2566604.
[61] A. M. Guarnieri and S. Tebaldini, "On the exploitation of target statistics for SAR interferometry applications," *IEEE Trans. Geosci. Remote Sens.*, vol. 46, no. 11, pp. 3436–3443, Nov. 2008, doi: 10.1109/TGRS.2008.2001756.
[62] M. Costantini, "A novel phase unwrapping method based on network programming," *IEEE Trans. Geosci. Remote Sens.*, vol. 36, no. 3, pp. 813–821, May 1998, doi: 10.1109/36.673674.
[63] R. M. Goldstein, H. A. Zebker, and C. L. Werner, "Satellite radar interferometry: Two-dimensional phase unwrapping," *Radio Sci.*, vol. 23, no. 4, pp. 713–720, Aug. 1988, doi: 10.1029/RS023i004p00713.
[64] D. C. Ghiglia and L. A. Romero, "Robust two-dimensional weighted and unweighted phase unwrapping that uses fast transforms and iterative methods," *J. Opt. Soc. Amer. A, Opt. Image Sci.*, vol. 11, no. 1, pp. 107–117, 1994, doi: 10.1364/JOSAA.11.000107.
[65] C. W. Chen and H. A. Zebker, "Phase unwrapping for large SAR interferograms: Statistical segmentation and generalized network models," *IEEE Trans. Geosci. Remote Sens.*, vol. 40, no. 8, pp. 1709–1719, Aug. 2002, doi: 10.1109/TGRS.2002.802453.
[66] A. Pepe, "Multi-temporal small baseline interferometric SAR algorithms: Error budget and theoretical performance," *Remote Sens.*, vol. 13, no. 4, p. 557, Feb. 2021, doi: 10.3390/rs13040557.
[67] P. S. Agram and M. Simons, "A noise model for InSAR time series," *J. Geophys. Res., Solid Earth*, vol. 120, no. 4, pp. 2752–2771, Mar. 2015, doi: 10.1002/2014JB011271.
[68] M. Manunta et al., "The parallel SBAS approach for Sentinel-1 interferometric wide swath deformation time-series generation: Algorithm description and products quality assessment," *IEEE Trans. Geosci. Remote Sens.*, vol. 57, no. 9, pp. 6259–6281, Sep. 2019, doi: 10.1109/TGRS.2019.2904912.
[69] A. Zheng, X. Chen, and W. Xu, "Present-day deformation mechanism of the northeastern Mina deflection revealed by the 2020 M_w 6.5 Monte Cristo range earthquake," *Geophys. Res. Lett.*, vol. 47, no. 22, Nov. 2020, Art. no. e2020GL090142, doi: 10.1029/2020GL090142.
[70] M. Neri, F. Guglielmino, and D. Rust, "Flank instability on Mount Etna: Radon, radar interferometry, and geodetic data from the southwestern boundary of the unstable sector," *J. Geophys. Res., Solid Earth*, vol. 112, no. B4, pp. 1–15, Apr. 2007, doi: 10.1029/2006JB004756.
[71] G. Solaro, V. Acocella, S. Pepe, J. Ruch, M. Neri, and E. Sansosti, "Anatomy of an unstable volcano from InSAR: Multiple processes affecting flank instability at Mt. Etna, 1994–2008," *J. Geophys. Res.*, vol. 115, no. B10, pp. 1994–2008, 2010, doi: 10.1029/2009JB000820.
[72] M. Duan et al., "Adaptively selecting interferograms for SBAS-InSAR based on graph theory and turbulence atmosphere," *IEEE Access*, vol. 8, pp. 112898–112909, 2020, doi: 10.1109/ACCESS.2020.3002990.
[73] A. Hooper and H. A. Zebker, "Phase unwrapping in three dimensions with application to InSAR time series," *J. Opt. Soc. Amer. A, Opt. Image Sci.*, vol. 24, no. 9, p. 2737, 2007, doi: 10.1364/JOSAA.24.002737.
[74] M. Costantini, F. Malvarosa, and F. Minati, "A general formulation for redundant integration of finite differences and phase unwrapping on a sparse multidimensional domain," *IEEE Trans. Geosci. Remote Sens.*, vol. 50, no. 3, pp. 758–768, Mar. 2012, doi: 10.1109/TGRS.2011.2162630.
[75] A. P. Shanker and H. Zebker, "Edgelist phase unwrapping algorithm for time series InSAR analysis," *J. Opt. Soc. Amer. A, Opt. Image Sci.*, vol. 27, no. 3, pp. 605–612, Mar. 2010, doi: 10.1364/JOSAA.27.000605.
[76] C. De Luca, F. Casu, M. Manunta, G. Onorato, and R. Lanari, "Comments on 'study of systematic bias in measuring surface deformation with SAR interferometry,'" *IEEE Trans. Geosci. Remote Sens.*, vol. 60, pp. 1–5, 2022, Art. no. 9100505, doi: 10.1109/TGRS.2021.3103037.

Francesco Falabella (Graduate Student Member, IEEE) received the B.Sc. degree in computer science and information technology and the M.Sc. degree (cum laude) in information technology and telecommunications engineering from the University of Basilicata, Potenza, Italy, in 2016 and 2019, respectively, where he is currently pursuing the Ph.D. degree in engineering for innovation and sustainable development.

In 2019, he joined the Institute for Electromagnetic Sensing of the Environment (IREA), Naples, Italy, and the Institute of Methodologies for Environmental Analysis (IMAA), National Research Council (CNR) of Italy, Tito, Italy, as a Research Associate. His research interests include synthetic aperture radar (SAR) data processing, ground-based SAR interferometry, advanced multitemporal interferometric SAR (InSAR) techniques, high-performance computing (HPC), and environmental remote sensing and applications.

Mr. Falabella received the Young Scientist Best Poster Award at the DRAGON 4 Mid-Term Results Symposium from the European Space Agency (ESA) and the Chinese Ministry of Science and Technology (MOST), Xi'an, China, in 2018.

Antonio Pepe (Senior Member, IEEE) received the Laurea degree in electronic engineering and the Ph.D. degree in electronic and telecommunication engineering from the University of Naples Federico II, Naples, Italy, in 2000 and 2007, respectively.

After graduation, following a short experience at Wind Telecommunication S.p.a., Rome, Italy, in 2001, he joined the Istituto per il Rilevamento Elettromagnetico dell'Ambiente (IREA), Italian National Research Council (CNR), Naples, where he currently holds a permanent position of a Senior Researcher. He was a Visiting Scientist with The University of Texas at Austin, Austin, TX, USA, in 2005; the Jet Propulsion Laboratory (JPL), Caltech, Pasadena, CA, USA, in 2009 and 2019; and East China Normal University (ECNU), Shanghai, China, from 2014 to 2019, under the High-End Foreign Experts Recruitment Program of the Chinese State Administration of Foreign Experts Affairs. From 2012 to 2017, he was an Adjunct Professor of signal theory with the Università degli Studi della Basilicata, Potenza, Italy. In 2018, he was an Adjunct Professor of mobile telecommunication systems with the University of Naples Federico II. His main research interests include the development of advanced differential synthetic aperture radar interferometry (DInSAR) algorithms for the monitoring of surface deformation phenomena induced by subsidence, volcano activities, and earthquakes, with a particular interest toward the phase unwrapping problems. More recently, he has developed research activities for the generation of DInSAR products through multiplatform/multiangle and the new generation synthetic aperture radar (SAR) instruments, the generation of hybrid scan SAR to stripmap DInSAR analyses, the integration of SAR and optical images, and the analysis of land changes in flooded areas.

Dr. Pepe was a recipient of the 2014 Best Reviewer Mention of the IEEE GEOSCIENCE AND REMOTE SENSING LETTERS and the 2017 Best Reviewer Mention of *Remote Sensing* (MDPI) journal. He acts as a reviewer for several peer-reviewed international journals.

Open Access funding provided by 'Consiglio Nazionale delle Ricerche-CARI-CARE' within the CRUI CARE Agreement